Optics & Laser Technology 157 (2023) 108713

Contents lists available at ScienceDirect

Optics and Laser Technology

journal homepage: www.elsevier.com/locate/optlastec

Full length article

Investigation of mechanical properties of laser welded dual-phase steels at macro and micro levels

Ekrem Öztürk [a,*], Hüseyin Arıkan [a]

[a] Department of Mechanical Engineering, Necmettin Erbakan University, 42370 Konya, Turkey

ARTICLE INFO

Keywords:
Dual-phase steel
Finite element
Laser welding
Micromechanical modeling
Microstructure
Tailor-welded blank

ABSTRACT

The current automotive industry uses new technology in materials processing and lightweight materials to minimize vehicle weight and fuel consumption. As a result, Tailor-Welded Blanks (TWB) are used in regions where additional strength or stiffness is necessary in body-in-white, thus decreasing weight. In this paper, TWB were produced by joining DP600 with 1.8 mm and DP800 with 0.8 mm and 1.5 mm using CO_2 laser welding. The effects of laser power and welding speed on the mechanical properties of TWB were investigated. The flow behaviors of the TWB were obtained from tensile tests. The microstructures of the weld zones of the base materials and TWB were revealed, and the numerical analyzes of the microstructures were performed by micromechanical modeling with a 2D representative volume element (RVE). Effective stress and plastic strain distributions in the microstructures and macroscopic flow curves of the base materials and the weld zones were obtained. The uniaxial tensile tests of the samples were modeled, and the flow behaviors of the TWB were obtained with micromechanical modeling. The results showed a significant change in stress distribution and strain localization depending on the grain size of constituents and the thickness ratios of the TWB at micro and macro scales, respectively. The numerical flow curves obtained using the RVE method were in good agreement with those of the experimental.

1. Introduction

Environmental concerns, climate change, and ever-decreasing fossil fuel stocks are some of the major reasons that forcing the automobile industry to control vehicle emissions and improve fuel efficiency. Considering the challenges of lighter vehicle weight to achieve emission norms without compromising passenger safety, the automobile industry is investigating steel grades such as advanced high-strength steels (AHSS) [1,2]. As the overall dimensions are expanding, the weight of automobiles has been constantly increasing since many electrical and electronic components have been included to meet the increasing demands on safety and comfort. To compensate for the weight of the additional components, the body-in-white should be lighter on vehicles, as higher weight leads to increased fuel consumption. Therefore, Tailor-Welded Blanks (TWB) are used only in areas where higher strength or stiffness is required in body-in-white [3,4]. TWB consist of two or more sheets of different thicknesses/strengths joined using any welding method. The desired parts can be obtained after forming these blanks [5].

One of the main joining methods used in the automotive industry is laser welding [6]. In the production of TWB, CO_2 ($\lambda = 10{,}600$ nm) and Nd: YAG ($\lambda = 1{,}064$ nm) are the most used welding methods. Advantages of laser welding include low heat input per unit volume, narrow fusion zone (FZ) and heat-affected zone (HAZ), low thermal distortion in the workpiece, high welding speed, and deep-narrow welding profiles [7,8].

As shown in Fig. 1, TWB account for about 15 % of an automobile body and are expected to increase by 25 %-30 % in the next 5–10 years [9]. Today, AHSS, which include dual-phase (DP), complex phase, and transformation-induced plasticity steels, are the most widely used steel sheets in the automotive industry. DP steels are highly preferred over other AHSS due to their excellent combination of strength and ductility, continuous yielding, and low production costs. The increase in the use of DP steels has led researchers to investigate the welding properties of these steels.

Several studies have been conducted to determine the mechanical properties of welded sheets. Kang et al. [11] reported in their study that Nd: YAG laser welded DP600 steel showed higher yield and tensile

* Corresponding author.
E-mail address: eozturk@erbakan.edu.tr (E. Öztürk).

https://doi.org/10.1016/j.optlastec.2022.108713
Received 19 July 2022; Received in revised form 24 August 2022; Accepted 21 September 2022
Available online 29 September 2022

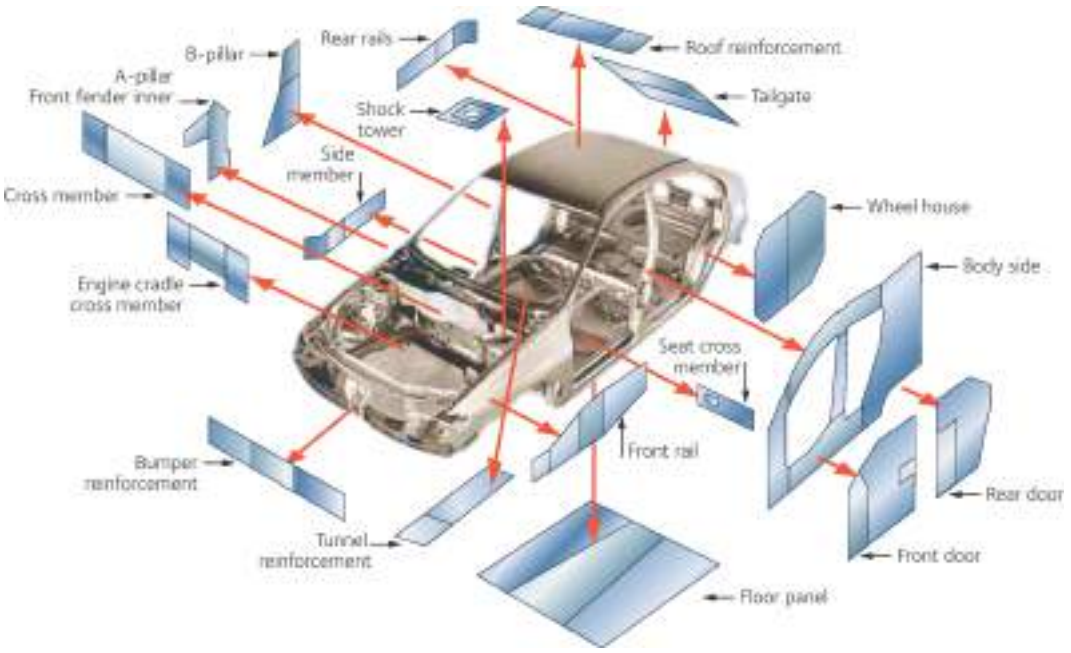

Fig. 1. Main applications of TWB in body-in-white [10].

Table 1
Chemical compositions of the dual phase steels used in the study (wt. %).

Material	C	Mn	Si	Cr	Mo	Al	Cu	Ni	S	N	P
DP600 1.8	0.097	1.5	0.361	0.598	0.003	0.049	0.018	0.118	0.011	0.018	0.04
DP800 1.5	0.12	2.04	0.31	0.523	0.0028	0.123	0.016	0.089	0.009	0.015	0.022
DP800 0.8	0.113	2.38	0.296	0.232	0.016	0.161	0.01	0.063	0.01	0.031	0.023

strengths compared to the base metal, but they reported that the total elongation of the welded sample decreased, and the damage occurred in the base metal, and they also concluded that the effect of softened HAZ was not evident in their study. Uchihara and Fukui [12] observed a similar fracture trend, however, in their study, the post-weld tensile strength decreased relative to the base metal. Sreenivasan et al. [13] performed tensile tests of laser welded DP980 steel and observed that both yield and tensile strength decreased after welding, and fracture always occurred in the outer region of the softened HAZ. A similar result was reported by Xia et al. [14], and it was stated that the effect of softened HAZ was more dominant at higher strength grades of DP steel.

Finite element (FE) micromechanical modeling through representative volume element (RVE) is commonly used to estimate the mechanical properties of DP steels numerically. Sun et al. [15] estimated the ductile damage behavior of DP980 steel in the form of plastic deformation localization, which occurs due to different deformation characteristics of the hard martensite phase and soft ferrite matrix. The failure modes and maximum ductility of DP steels were investigated under different loading conditions using microstructure-based FE modeling. They observed that the local damage mode was related to the stress state in the material. Sun et al. [16] investigated the key factors affecting ductile damage in DP600, DP780, and DP980 steels with a microstructure-based modeling approach. They found that the ductility of DP steels depended on the ductility of the ferrite matrix, microvoids, and martensite volume fraction (MVF). Ramazani et al. [17] investigated the onset of damage in DP steel. They used the microstructure-based RVE method to evaluate the deformation in the microstructure. They determined that fracture in martensite is the main damage initiation mechanism in DP steel. Wei et al. [18] used a micromechanical modeling-based approach through 2D RVE to predict the yield behavior and plastic deformation of DP600 steel. They observed that the martensite phase inhibited the material flow between the ferrite matrix, owing to the tensile-bending-effect test used with the microstructural 2D RVE modeling. They also determined that this phenomenon increases the strength of the steel thanks to the high stress localization. So far, few numerical studies have been conducted on the mechanical properties of TWB. Ramazani et al. [19] conducted a study on the microstructure analysis of the welding zones of DP600 steel. They used the macro-mechanical FE model to simulate the mechanical properties of welded tensile specimens. They emphasized that the 2D RVE model cannot accurately predict the yielding behavior of the material. Therefore, they used empirically obtained stress relations based on 2D to 3D conversion developed by Ramazani et al. [20]. They determined that the experimental and numerical flow curves were compatible with each other. Moeini et al. [2] used the 2D RVE method to predict the fatigue behavior of laser-welded DP600 steel. The cyclic behavior of ferrite and martensite phases in different weld zones was calculated with a dislocation-density-based model. They found that the fatigue weak region of laser-welded steel could be estimated well with the micro-mechanical model. The present literature shows that studies on the micromechanical modeling of TWB are extremely limited. The main aim of this study was to investigate the mechanical properties of TWB joined by CO_2. This is achieved by revealing all microstructures in weld zones and using them in the 2D RVE model. Since dissimilar materials being joined play a significant role in the performance of the TWB, stress and strain distributions are obtained in all weld zones. Finally, macro-mechanical responses of TWB are predicted with an FE model and compared with those obtained from experiments.

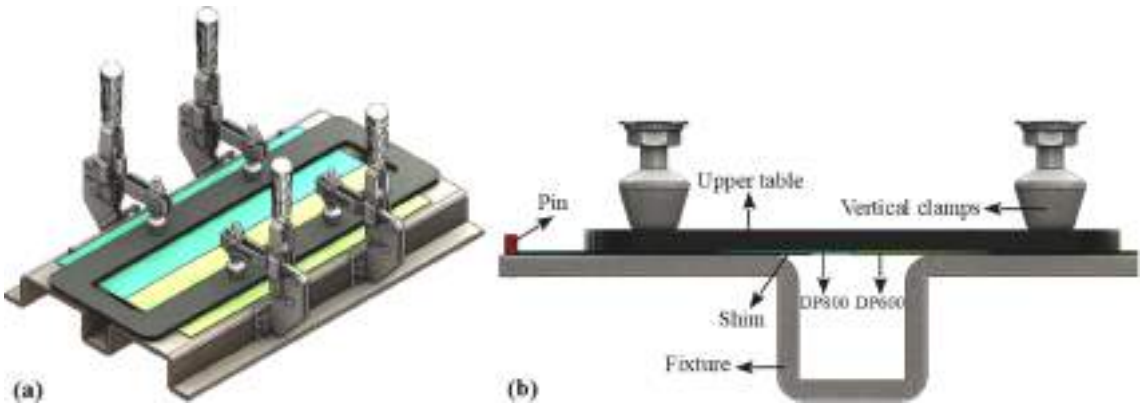

Fig. 2. Different views of the designed fixture (a) isometric, (b) front.

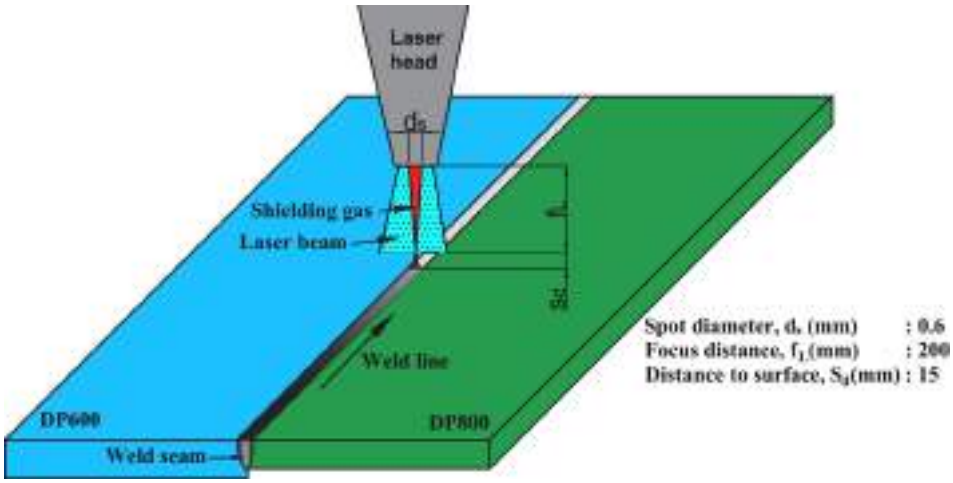

Fig. 3. Schematic representation of the CO_2 laser welding process.

Table 2
Welding parameters used in the study.

Laser Power, P (kW)	Welding Speed, S (m/min)	Shielding Gas (%100)	Shielding Gas Flow Rate (L/min)
2–3	3–4	Argon	10

2. Experimental design

2.1. Definition of base material

To produce TWB in this study, hot-dip galvanized and hot-rolled DP600 steel with a thickness of 1.8 mm and DP800 steels with thicknesses of 1.5 mm and 0.8 mm were used. The chemical compositions of the steels are presented in Table 1. The investigated DP steels have low carbon contents with high Mn, Si, and Cr contents.

2.2. Laser welding details

A fixture was manufactured after bending a 10 mm sheet in the CNC press brake and finishing surface in the CNC vertical machining center to make precision alignment of the surfaces on which the sheets are placed. The designed fixture is depicted in Fig. 2. To ensure that the top surfaces of the sheets with different thicknesses placed on the fixture were aligned, a shim was used under the thinner sheet (DP800). Two pins were used to center the sheets on the fixture. Also, to prevent fluctuations during welding, an upper table was placed on both sheets and fixed by four vertical clamps mounted on the sides of the fixture. Thanks to this design, sheet materials were easily placed and fixed on the fixture in all welding operations.

Laser welding of DP steel sheets was conducted using a Trumpf Truflow CO_2 laser unit and a TruLaser Cell 1050 CO_2 laser welding machine. The maximum output power of the laser unit was 4 kW and the machine operated in continuous wave mode. Fig. 3 shows a schematic representation of the CO_2 laser welding process. The spot diameter (d_s) shows the diameter of the beam reflected from the focus lens in the laser head. The focal length (f_L) is the distance of the laser beam from the lens to the point of focus. The distance of the unfocused laser beam to the sheet surface (S_d) was taken as 15 mm in all welding operations. In welding processes, different welding parameters were used to examine the mechanical and microstructural changes of the welded joint. Laser power (P) and welding speed (S) were chosen as the variable parameters. The welding parameters used in the welding processes are given in Table 2. Laser powers of 2 kW and 3 kW, and welding speeds of 3 m/min and 4 m/min were used to avoid cutting and penetration issues. In all welding processes, 100 % pure Argon was used as a shielding gas and the gas flow rate was taken as 10 L/min.

DP600 with 1.8 mm and DP800 with 1.5 mm and 0.8 mm were butt welded with the CO_2 laser welding method and TWB with a thickness ratios of 1.2 (1.8/1.5) and 2.25 (1.8/0.8) were produced. In the next chapters, Tailor-Welded Blanks DP600 1.8-DP800 1.5 and DP600 1.8-DP800 0.8 are nominated as TWB1 and TWB2, respectively.

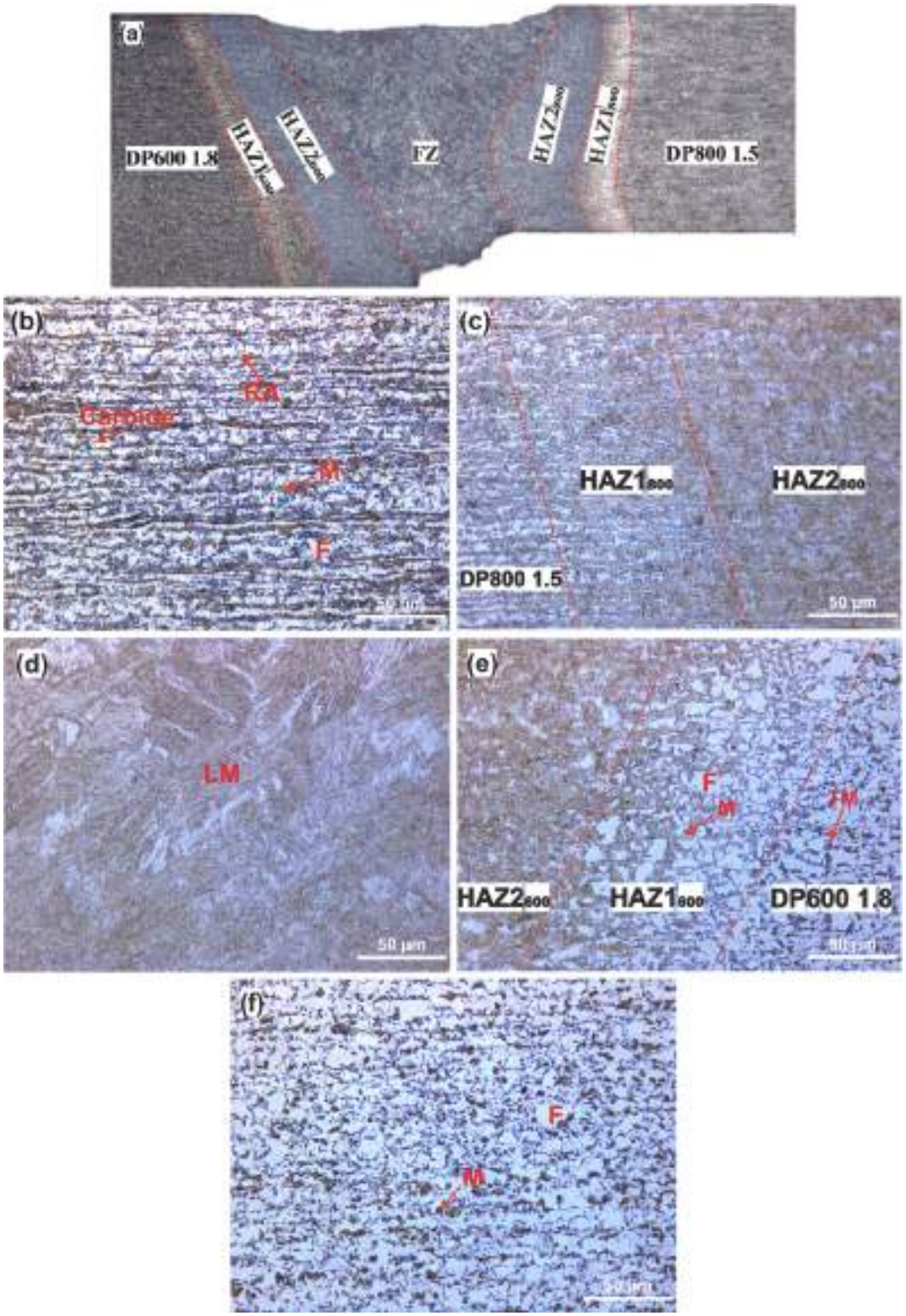

Fig. 4. OM images of the weld zone of TWB1 joined at P3S3, (a) macroscopic view of the cross-section, (b) DP800 1.5, (c) $HAZ1_{800}$ + $HAZ2_{800}$, (d) FZ, (e) $HAZ1_{600}$ + $HAZ2_{600}$, (f) DP600 1.8 (F: ferrite, M: martensite, LM: lath martensite, RA: retained austenite, TM: tempered martensite).

2.3. Microstructural characterization

All metallographic samples were cut from the welded sheets with the weld line in the middle using an abrasive cutting device with water cooling. The sectioned samples were then cold-mounted in epoxy resin. For microscopic examinations, the samples were first sanded with SiC-based sandpaper of 400, 800, and 1200 grit, respectively. The surfaces of the samples were then polished using 6, 3, and 1 μm polycrystalline diamond paste, respectively, and finally etched with 2 % nital for 5 s to reveal the microstructures.

Fig. 4 and Fig. 5 represent the optical microscope (OM) images of the macrostructure of the TWB1 and TWB2 along with the microstructures

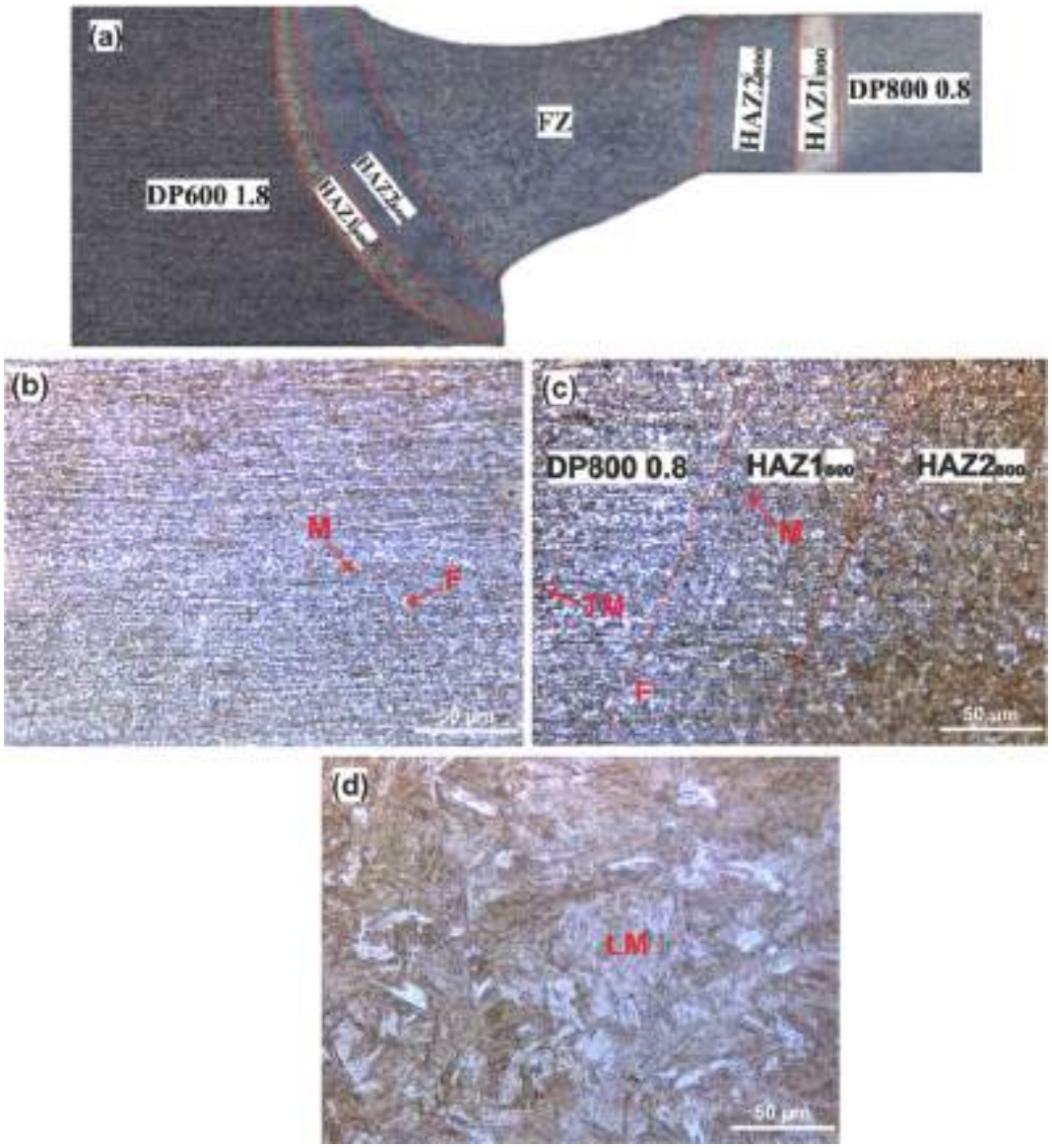

Fig. 5. OM images of the weld zone of TWB2 joined at P3S3, (a) macroscopic view of the cross-section, (b) DP800 0.8, (c) HAZ1 + HAZ2 of DP800 0.8, (d) FZ (F: ferrite, M: martensite, LM: lath martensite, TM: tempered martensite).

in different zones in the weld joint, which were joined with a power of 3 kW and a speed of 3 m/min (P3S3). Other welding parameters follow the same microstructural changes as the P3S3 and thus are not given in the study. Macroscopic images show conical-shaped FZs, which were formed after the melting and solidification of the metal exposed to high heat input. FZs are usually conical in shape due to the keyhole phenomenon in high-power laser welding processes [21]. As different temperature gradients are induced on the workpiece during laser welding and the microstructure is locally deteriorated depending on the cooling rate, different weld zones were formed in the welding joint. The microstructure of the FZ is lath martensite (LM) due to the rapid cooling in this zone.

The heat input decreases gradually moving away from the FZ, resulting in a lower cooling rate in these regions. The HAZ1s next to the FZ reached above the A_3 temperature, where the austenite completely transformed into plate martensite with a high cooling rate. The temperature of the HAZ2s remained between the A_1-A_3 temperatures, where the austenite + ferrite phases are located, and the entire austenite plate in the microstructure transformed into plate martensite, despite the relatively lower cooling rate compared to HAZ1s (Fig. 4c and e). Therefore, apart from the MVFs, the HAZ2s have the same microstructure as the base materials. Additionally, since the maximum temperature of the region in the base material was below the A_1 temperature, no austenite phase was formed and thus the martensite was tempered (Fig. 4e and Fig. 5c). The tempering degree of martensite was low because of the rapid cooling rate. This softened HAZ could not be distinctly seen on OM images. The HAZ1 and HAZ2 are named as "$HAZ1_{600}$-$HAZ2_{600}$", and "$HAZ1_{800}$-$HAZ2_{800}$" to distinguish the HAZs in DP600 and DP800 sheets, respectively.

In the regions far from the FZ, no changes were present in the microstructures of the base materials (ferrite + martensite) since there was no heat input from the laser beam. The microstructure of DP600 1.8 consists of small polygonal martensite islands within the polygonal ferrite matrix (Fig. 4f), while the microstructure of both DP800 base materials consists of heterogeneously distributed parallel bands of ferrite matrix and martensite islands in the rolling direction (Fig. 4b and Fig. 5b). Also, all base materials have finely dispersed carbide precipitates in their microstructures.

As some of the high-density energy could not be transferred to the workpiece by the laser beam during the welding of the TWB2 with a high

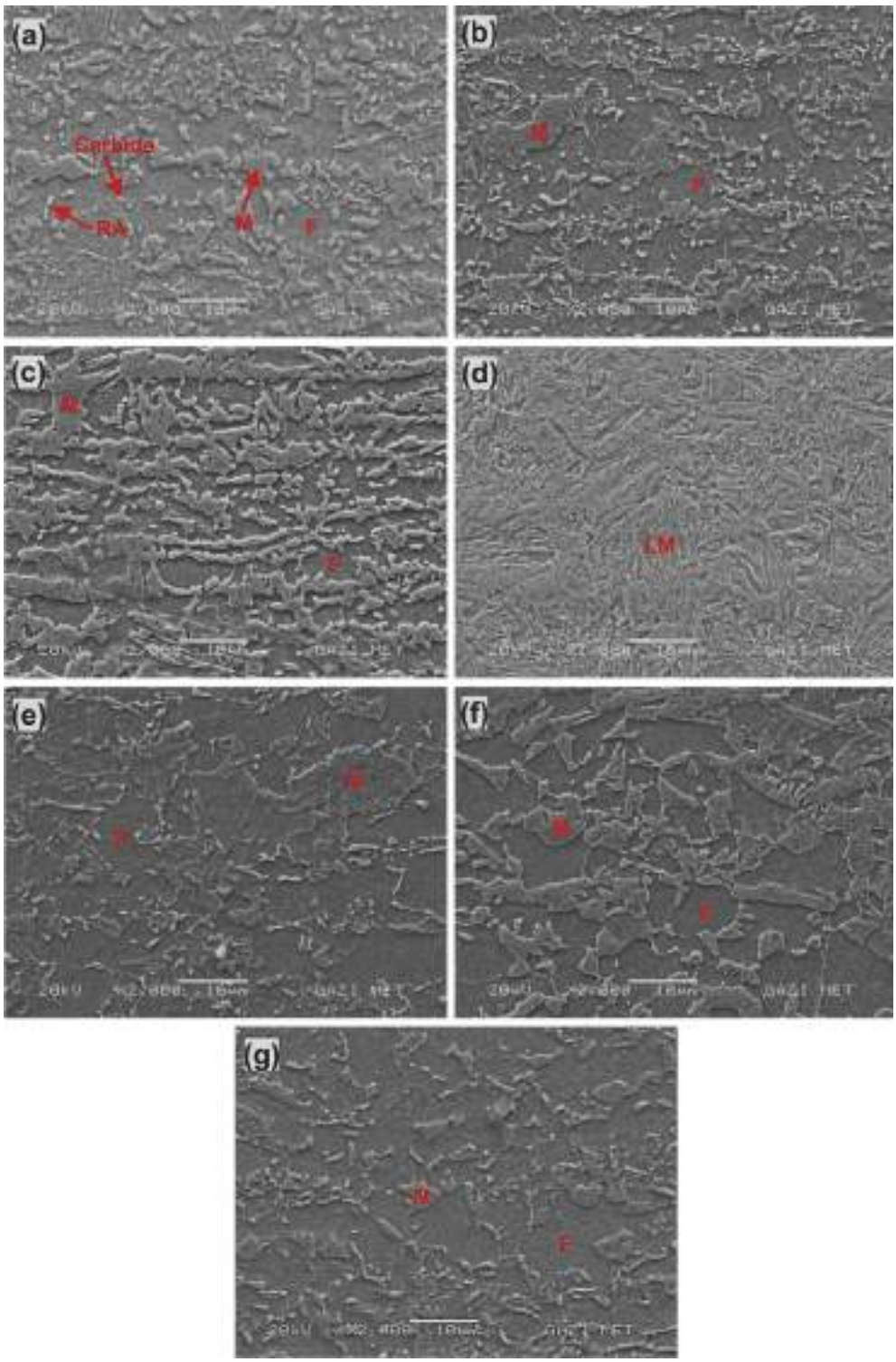

Fig. 6. SEM images of the weld zone of TWB1 joined at P3S3, (a) DP800 1.5, (b) $HAZ1_{800}$, (c) $HAZ2_{800}$, (d) FZ, (e) $HAZ1_{600}$, (f) $HAZ2_{600}$, (g) DP600 1.8 (F: ferrite, M: martensite, LM: lath martensite, RA: retained austenite).

thickness difference, the $HAZ1_{600}$ and $HAZ2_{600}$ in the DP600 1.8 base material changed from a linear form (Fig. 4a) to a circular form (Fig. 5a). This indicates that the laser beam energy transfer depends heavily on the thickness of the joined parts.

Fig. 6 and Fig. 7 show the scanning electron microscope (SEM) micrographs of the weld zones of TWB1 and TWB2, respectively. No bainitic structure was observed in all zones, which is difficult to distinguish in the OM examinations. The reason why the bainitic structure was not formed in HAZs and FZs is that the welding parameters used in the study cause rapid cooling rates that do not allow the austenite to transform into bainite. Some scattered retained austenite (RA) and carbide precipitates are also present in the base materials. (Fig. 6a, g, and Fig. 7a). Tempered martensite in the base material can also clearly be seen in DP800 1.5 in Fig. 6a. Note that the thermal cycle during welding results in a banded structure in the HAZ2s (Fig. 6c, f, and Fig. 7c). The mechanism behind this phenomenon is attributed to the microsegregation of

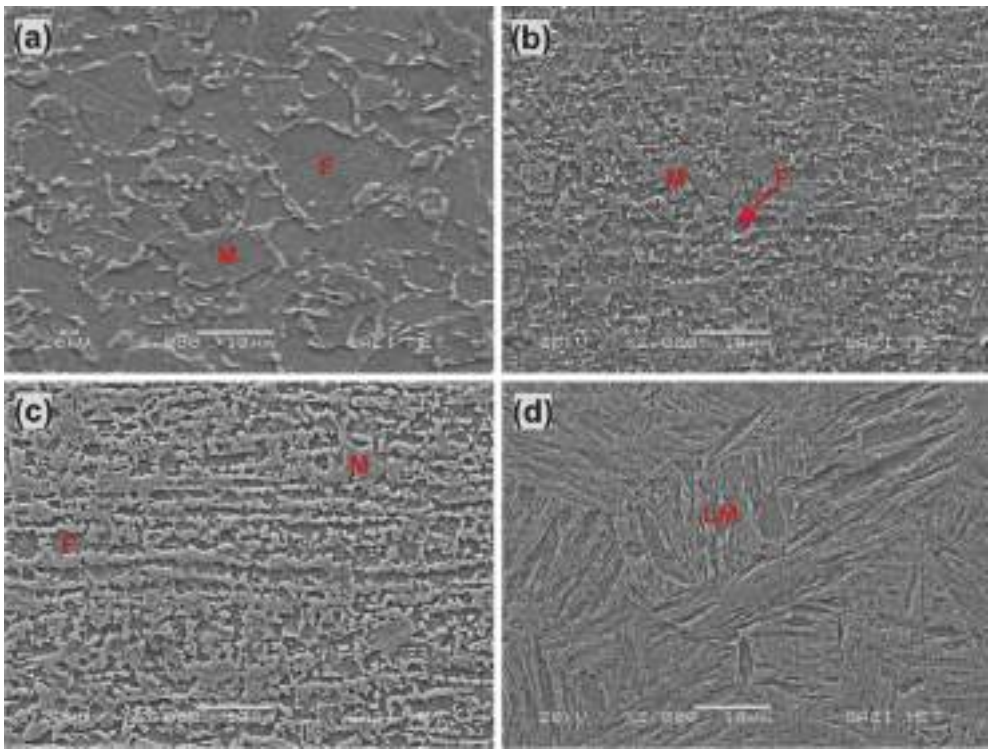

Fig. 7. SEM images of the weld zone of TWB2 joined at P3S3, (a) DP800 0.8, (b) $HAZ1_{800}$, (c) $HAZ2_{800}$, (d) FZ (F: ferrite, M: martensite, LM: lath martensite).

Table 3
Volume fractions of the phases in base materials.

Base Material	Micrograph (ASTM E562)	Digitization (ImageJ)
DP600 1.8		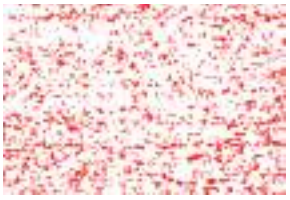
	Martensite: 16.9295 % CI: 1.83 Ferrite: 83.08RA %: 10.82	Martensite: 16.95 Ferrite: 83.05
DP800 1.5		
	Martensite: 37.7095 % CI: 2.49 Ferrite: 62.30RA %: 6.61	Martensite: 37.70 Ferrite: 62.30
DP800 0.8		
	Martensite: 45.6795 % CI: 3.18 Ferrite: 54.33RA %: 6.96	Martensite: 45.61 Ferrite: 54.39

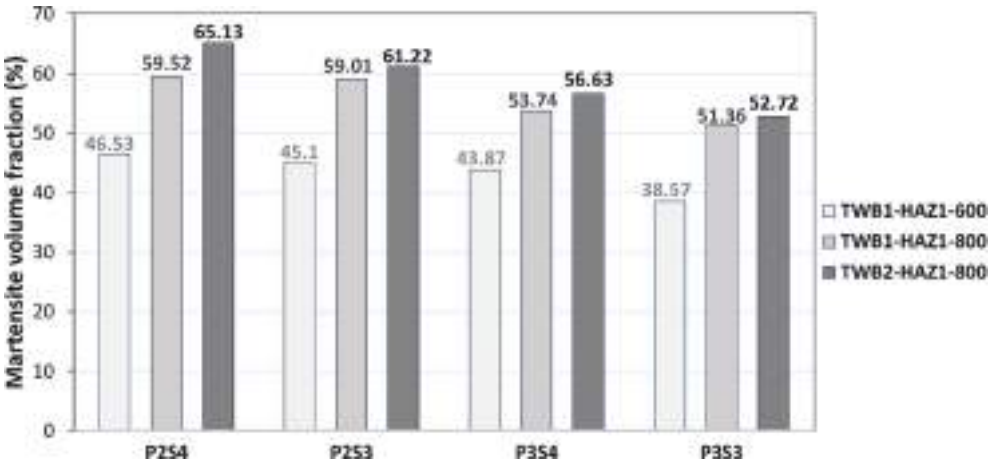

Fig. 8. Effect of laser welding parameters on martensite volume fractions in the HAZ1s of TWB1 and TWB2.

Table 4
Average ferrite grain size in the base materials.

Base Material	Ferrite (μm)	95 % CI (%)	RA (%)
DP600 (1.8)	4.42 ± 2.19	2.19	2.63
DP800 (1.5)	2.62 ± 3.23	3.23	5.20
DP800 (0.8)	1.60 ± 5.21	5.21	9.60

the alloying elements, especially Mn and Si, during solidification [22,23] (see Table 1 for the alloying elements of the base materials).

2.3.1 Volume. fractions of the phases

The volume fractions of the phases were determined manually by ASTM Standard E562 [24]. An image processing software ImageJ [25] was also used to compare results with the manual method. The micrographs were digitized by taking advantage of the contrast difference in the phases. Table 3 shows a comparison of the phase fractions determined by ASTM E562 and ImageJ. A statistical precision of 20 % (relative accuracy, RA) and thus, six fields were chosen for 100 grid points. The resultant 95 % confidence interval (CI) and the RA remained within acceptable limits in all microstructures. The low RA values indicate that the measurements, that is, the average phase volume fractions, are close to each other and the repeatability is good. The MVFs in the digitized micrographs are almost identical to those in the manual method. Moreover, the microstructural constituents (red martensite islands) in the digitized micrographs are very similar in shape to those in undigitized micrographs. This comparison shows both the accuracy of the manual method and the digitization process.

The heat input generated during laser welding varies depending on the laser power and the welding speed. When the focal distance is constant, the heat input is expressed by the following equation:

$$\text{Heat input (J/mm)} = \frac{\text{Laser power (W)}}{\text{Welding speed (mm/s)}} \quad (1)$$

The laser heat input resulting from the effect of the laser power (P) and the welding speed (S) was calculated as 30, 40, 45, and 60 J/mm for the welding parameters P2S4, P2S3, P3S4, and P3S3, respectively. As can be seen, the lowest heat input was obtained in the P2S4 welding parameter, where the laser power was the lowest and the welding speed

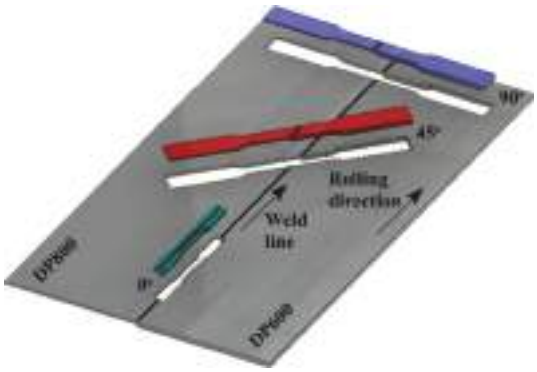

Fig. 10. Schematic representation of the tensile test specimens cut from TWB.

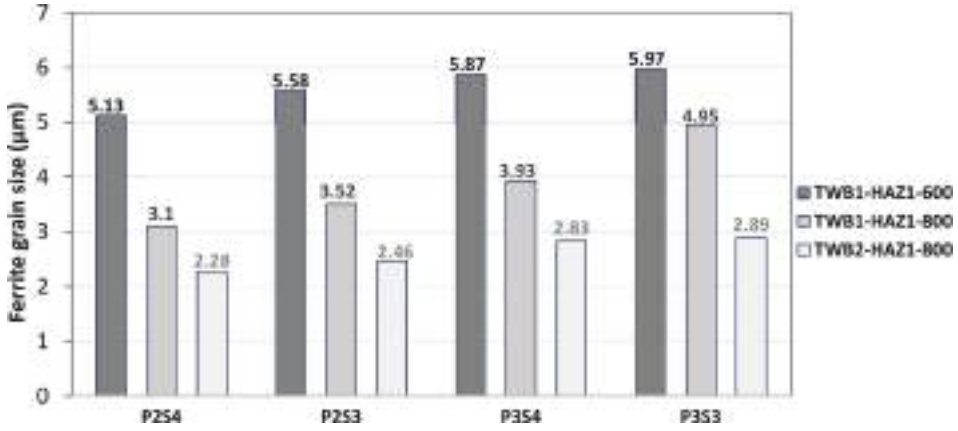

Fig. 9. Effect of laser welding parameters on ferrite grain sizes in the HAZ1s of TWB1 and TWB2.

Fig. 11. Fracture images of the base materials after tensile tests.

was the highest.

Fig. 8 shows the effect of laser heat input on MVF in HAZ1s after welding. It can be seen that the MVF decreased in both HAZ1s with the increase of laser heat input. Higher heat input decreased the rate of transformation from austenite to martensite by decreasing the cooling rate, resulting in lower MVF. The MVFs of the HAZ1s are higher than the base materials. The highest MVF (65.13 %) is in $HAZ1_{800}$ of the TWB2 due to the lowest heat input in P2S4 and the highest MVF of the DP800 0.8 base material.

2.3.2. Grain size of the ferrite

The grain sizes of the ferrite phase were measured with the linear interception method by ASTM Standard E112 [26]. Average ferrite grain sizes obtained for the base materials are given in Table 4. It can be seen that the average ferrite grain sizes are 4.42 μm, 2.62 μm, and 1.60 μm for DP600 1.8, DP800 1.5, and DP800 0.8, respectively. These values indicate that the DP steels are fine-grained. Since DP800 1.5 and DP800 0.8 contain banded microstructures and have smaller grain sizes, the RA values were higher than those of DP600 1.8 steel. However, the RA values obtained from statistical analysis did not exceed the target value of 10 %.

The ferrite grain sizes in HAZ1s of the TWB1 and TWB2 are shown in Fig. 9. The results show that the ferrite grain sizes in $HAZ1_{600}$ and $HAZ1_{800}$ increase slightly with laser heat input. The highest grain size was determined as 5.97 μm and 4.95 μm in P3S3 of TWB1, which has the highest heat input, respectively. When the grain sizes in $HAZ1_{800}$ are compared for the same welding parameters in Fig. 9, there is a difference between the ferrite grain sizes. This is due to the different prior ferrite grain sizes in the base materials. Additionally, despite the low heat input, laser welding caused ferrite grain sizes in HAZ1s to be obtained above the grain sizes of the base materials.

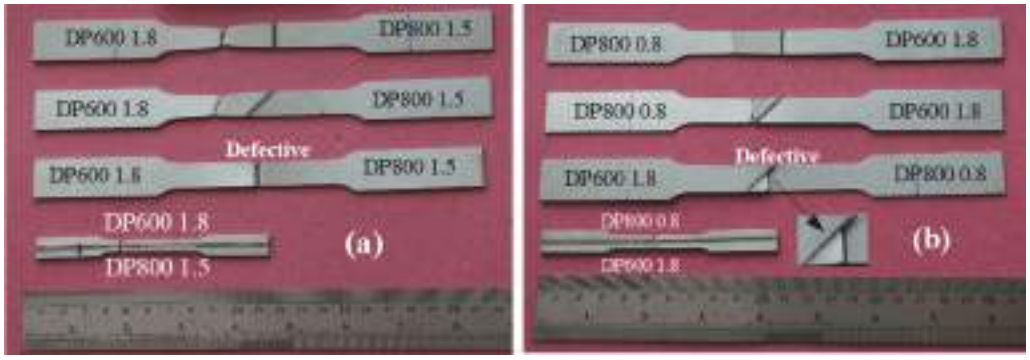

Fig. 12. Fracture images after tensile tests (a) TWB1, (b) TWB2.

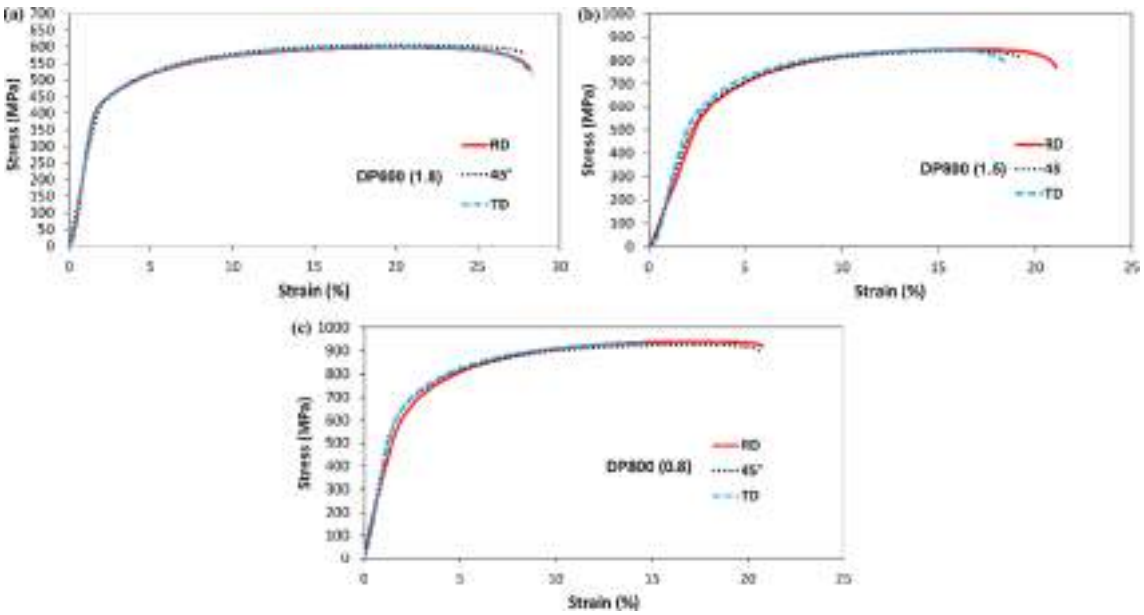

Fig. 13. Stress–strain curves of the base materials (a) DP600 1.8, (b) DP800 1.5, (c) DP800 0.8.

Table 5
Mechanical properties of the base materials in the rolling direction.

Base Material	Yield strength (MPa)	Ultimate tensile strength (MPa)	Uniform elongation (%)	Total elongation (%)	Strain hardening exponent, n	Strength coefficient, K (MPa)
DP600 1.8	418	598	18.52	28.75	0.224	1047
DP800 1.5	562	846	16.92	21.32	0.276	1687
DP800 0.8	580	940	17.38	20.98	0.260	1820

2.4. Tensile tests

For uniaxial tensile tests, base materials and TWB were cut according to ASTM Standard E8 [27]. The base materials were cut to be perpendicular (90°) to the rolling direction (RD), at an angle of 45° (45°), and in the tensile direction (0°). TWB were cut in such a way that the weld metal was in the middle. While base materials and TWB of 90° and 45° were cut to the standard dimensions, TWB of 0° were cut to the sub-size dimension of the related standard.

Cutting of the tensile test specimens from TWB is shown schematically in Fig. 10. This cutting style enables us to cut many tensile test specimens in all three directions from the TWB. The welding direction and the rolling direction of the sheets were taken the same in all three directions.

Uniaxial tensile tests of tensile test specimens were performed in Shimadzu AGS-X tensile tester with a maximum tensile load of 100 kN. The tests were carried out at a crosshead speed of 2 mm/min. Since this crosshead speed produces a $6.6x10^{-4}$ s^{-1} deformation rate, it can be said that the tests were carried out at a quasi-static rate. The main reason for performing tests in different welding directions in this study was to determine the welding performance and mechanical properties of the samples in each direction. In all tensile tests, each sample was carefully fixed to the tensile tester. Special attention was paid especially to the welded samples to avoid the bending effect due to the thickness difference. For this reason, for the tensile tests of the specimens where the welding line is 0° to the tensile direction, a sheet with a thickness that was equal to the thickness difference of the welded materials was bonded on the thin sheet.

Tensile tests were carried out on the base materials in the rolling direction (RD) and at an angle of 45° to the rolling direction and transverse direction (TD). In Fig. 11, only the fracture images obtained after the tensile tests in the TD are given. The formation of the slip lips and thus the ductile fracture can be seen in DP600. It can be seen that the DP800 1.5 has a fracture angle of 72° to the tensile direction. However, brittle fracture occurred at an angle of 90° to the tensile direction in the same material with less thickness (DP800 0.8 mm).

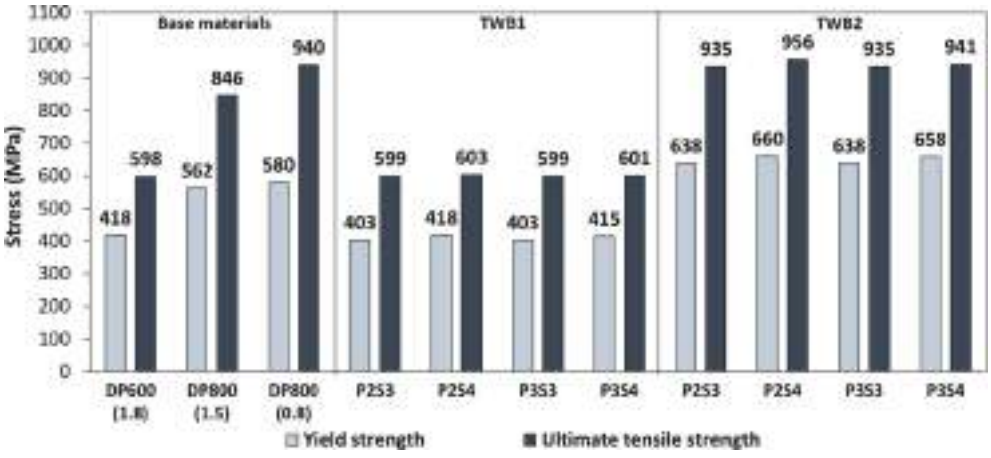

Fig. 14. Comparison of yield and ultimate tensile strengths of the base materials and TWB.

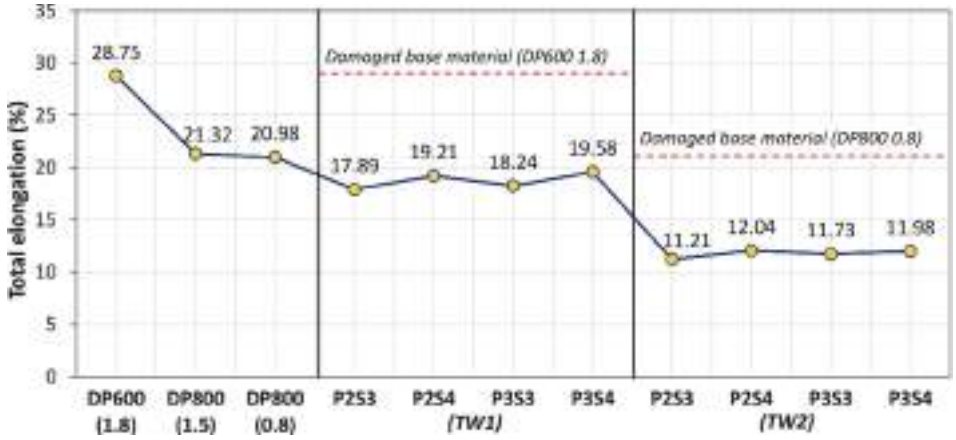

Fig. 15. Comparison of total elongation of the base materials and TWB.

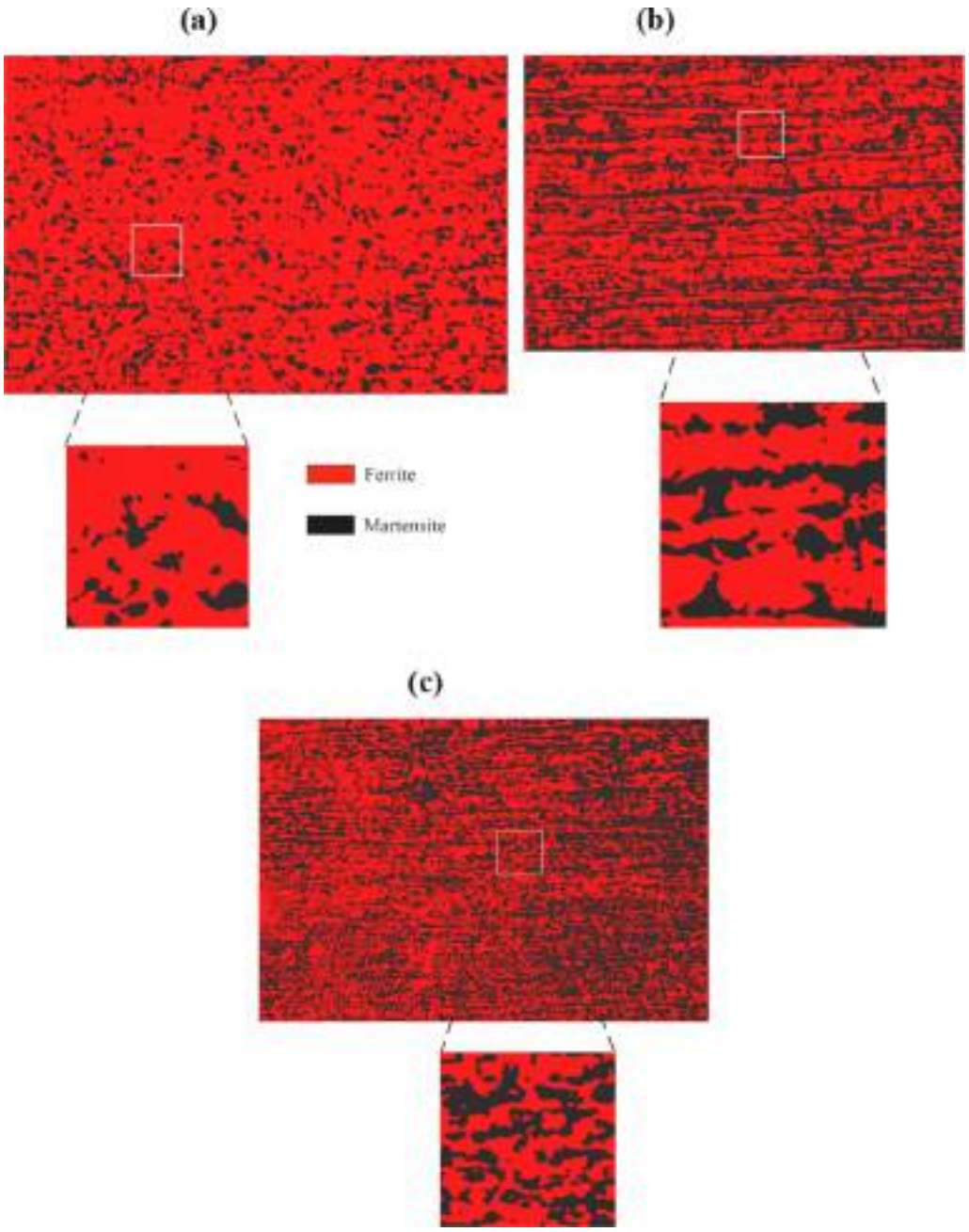

Fig. 16. RVEs selected from the real microstructures of (a) DP600 1.8, (b) DP800 1.5, (c) DP800 0.8.

Regardless of the welding parameters, damage occurred in the base materials DP600 1.8 and DP800 0.8 for the TWB1 and TWB2, respectively. In Fig. 12, the fracture images of the TWB1 and TWB2 welded at P2S4 are shown. Defective specimens are also presented, which were fractured in the weld metal in different directions due to the pores formed in the welding zone during the welding process. In 45° specimens of TWB1, it is seen that the damage occurred at an angle of 45° to the tensile direction since the rolling direction was taken the same as the welding direction (Fig. 12a), whereas the damage propagated perpendicular to the tensile direction in 45° specimens of TWB2 (Fig. 12b). Although both materials were subjected to the same load in 0° specimens, different stresses occurred due to the different cross-sections of the joined materials. In these specimens, the rupture first occurred in DP600 in the form of slip lips and then it proceeded perpendicular to the tensile direction in DP800.

2.4.1. Mechanical properties of the base materials

All tensile tests were performed to achieve three successful results. Engineering stress–strain curves obtained after uniaxial tensile tests of the base materials are shown in Fig. 13. The stress–strain curves were plotted by averaging the three repetitions. All base materials show a continuous yielding. The reason for the continuous yielding of DP steels is the high-density mobile dislocations and residual stresses in the ferrite matrix at the martensite boundary formed during the cooling stage in the production of DP steels [28]. DP600 has the maximum total elongation (TE), and due to the equiaxed homogeneous phases in its microstructure, the TEs are almost the same in all three directions, making it an isotropic material. However, the TEs of the base materials DP800 have some dependency on directions due to the banded phases in their microstructures. Additionally, the yield strength (YS) and ultimate tensile strength (UTS) values of all base materials were close in all three directions. Although the base materials DP800 have elongated grains in

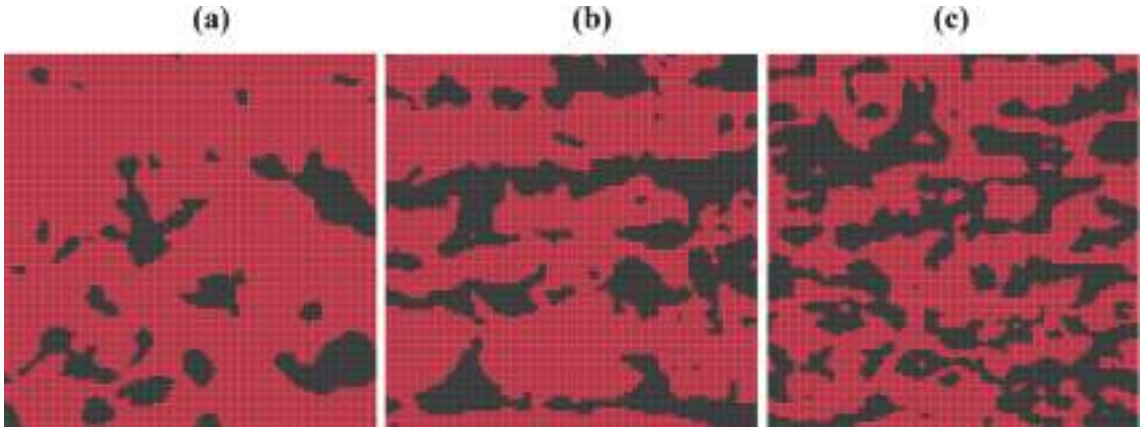

Fig. 17. Generated mesh structures of RVEs selected from the real microstructures of (a) DP600 1.8, (b) DP800 1.5, (c) DP800 0.8.

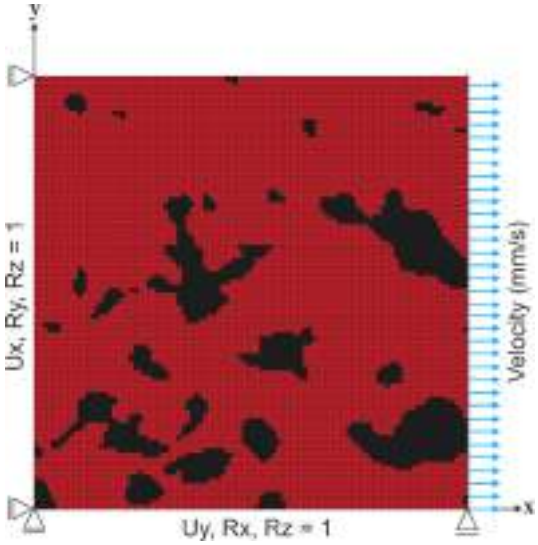

Fig. 18. Periodic boundary conditions of the 2D RVE.

their microstructure, the YS and UTS values were almost same perhaps owing to their high martensite volume fractions, compensating the response of the initial crystallographic orientation. From this, it can be concluded that the morphologies of the phases in the microstructure are more dominant on TE.

It was assumed that the plastic deformation of all materials follows the power-law hardening (Hollomon). Hollomon's equation is expressed as below:

$$\sigma = K.\varepsilon^{n} \quad (2)$$

where, n and K are the hardening exponent and strength coefficient, respectively, and ε is the true strain. The homogeneous plastic strain region in the true stress–strain curve of the material is characterized by this equation. To this end, true stress–strain curves of all materials were plotted, and the values of n and K were calculated by linear regression using the least square method. In all regression analyzes, the minimum coefficient of determination (R^2) was calculated as 0.975.

A detailed comparison of the mechanical properties of the base materials in the rolling direction is presented in Table 5. Since all materials had continuous yielding, the yield strengths were determined at a strain of 0.2 %. DP800 0.8 has the highest YS and UTS. It also had the minimum difference in total and uniform elongation. It is obvious that this material fractured suddenly after reaching its UTS (Fig. 13c). This corresponds well with the brittle fracture mechanism in this material. The YS values of DP800 1.5 and DP800 0.8 are 562 MPa and 580 MPa, respectively. A slight difference between the YS values is due to the similar grain sizes of these materials. However, the TS values of DP800 1.5 and DP800 0.8 are 846 MPa and 940 MPa, respectively. The TS value of the base materials highly depends on the MVF, a well-known phenomenon in DP steels [29,30]. The fact that the DP800 0.8 material has a lower n value than that of DP800 1.5 is due to the higher MVF of the former material. This result agrees well with the findings of Zhang et al. [31].

YS and UTS values obtained as a result of uniaxial tensile tests of the base materials and the TBWs are given in Fig. 14. Although damage occurred in the base materials in all welding parameters, YS and UTS values of TWB1 change slightly compared to the values of the base material where damage is present (DP600). However, the YS value of the TWB2 is much higher than that of the damaged DP800 0.8 base material. The welding parameter P2S4, which has the highest cooling rate, yields the highest YS and UTS values in both TWB1 and TWB2.

The TE values obtained after uniaxial tensile tests of the base materials and TBWs are compared in Fig. 15. It can be seen that the TE values for all welding parameters are lower than the values of the damaged base material. Also, the effect of the welding parameters on the TE is unsubstantial. The welding parameters with the highest TE of 19.58 % and 12.04 % in TWB1 and TWB2 are P3S4 and P2S4,

Table 7
Values of parameters in the strain-dependent term in Eq. (3).

Base Material	$T_{annealing}$ (°C)	C_f (%)	C_m (%)
DP600 1.8	708	0.0061	0.543
DP800 1.5	738	0.0049	0.310
DP800 0.8	748	0.0043	0.242

Table 6
Values of parameters in the strain-dependent term in Eq. (3).

Taylor factor M	Shear modulus μ (MPa)	Burgers vector b (m)	Constant α	Phase	Recovery rate k_2	Dislocation mean free path L (m)
3	80,000	$2.5x10^{-10}$	0.33	Ferrite	$k_2 = 10^{-5}/d_\alpha$	$L = d_\alpha$
				Martensite	$k_2 = 41$	$L = 3.8x10^{-8}$

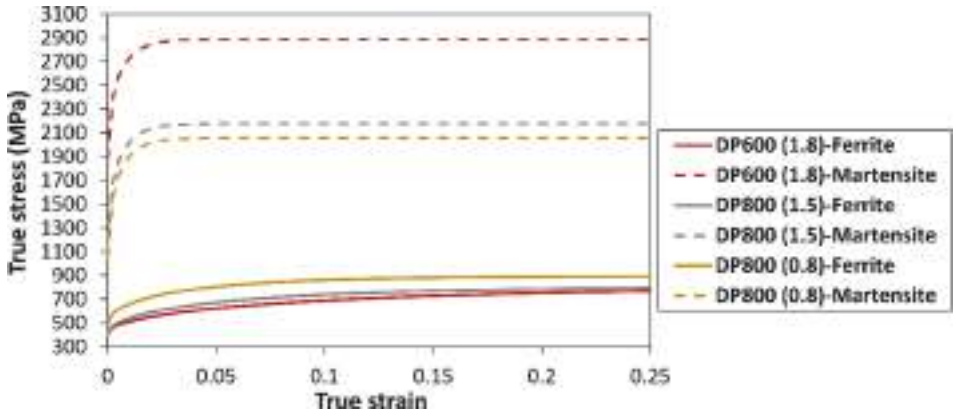

Fig. 19. Analytical flow curves of ferrite and martensite in the base materials.

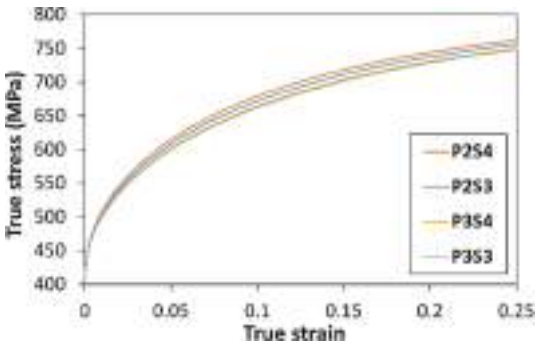

Fig. 20. Analytical flow curves of ferrite in the $HAZ1_{600}$ of TWB1 at different welding parameters.

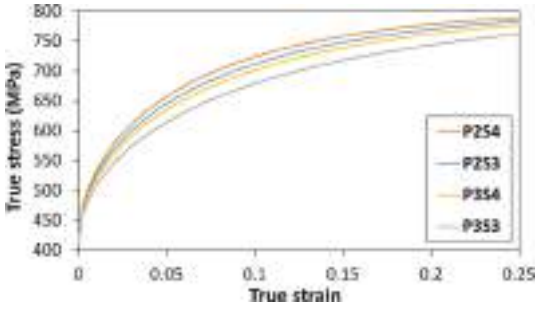

Fig. 21. Analytical flow curves of ferrite in the $HAZ1_{800}$ of TWB1 at different welding parameters.

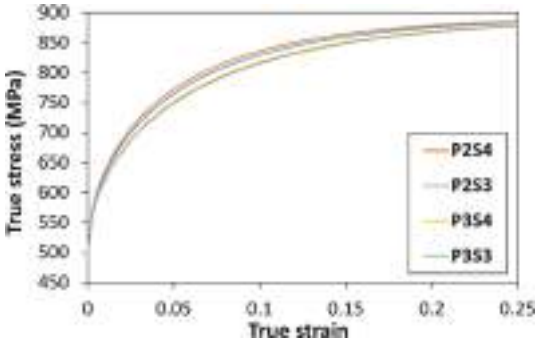

Fig. 22. Analytical flow curves of ferrite in the $HAZ1_{800}$ of TWB2 at different welding parameters.

respectively. When the TWB1 and TWB2 are compared, although they are exposed to the same load during the tensile test, the stress formed in DP800 0.8 with a lower cross-sectional area is higher.

3. Finite element simulation

One of the main advantages of the laser welding process is the reduced thermal energy induced on the joined materials. Even though this improves the welding quality, some restrictions are put on the examination of the mechanical properties of the weld metal due to the lower HAZs and FZ. A more advantageous and cost-effective method is FE simulation to overcome these limitations. Therefore, a real microstructure-based micromechanical modeling technique was used to study the mechanical properties. 2D micromechanical models with representative volume element (RVE) were developed to predict the flow behavior of the base materials and TWB using Ls-Dyna FE software.

3.1. Representative volume element generation

The geometric definition of the RVE was performed using the shape, size, and distribution of the microstructural constituents. An RVE should include different phases to represent the heterogeneity of the DP steels. In this study, all base materials consisted of a soft ferrite matrix dispersed with hard martensite islands. TWB have distinct HAZ1s-HAZ2s and base material with softened HAZ. These narrow zones were also included in the RVEs and named "Softened HAZ1" for DP600 1.8 and "Softened HAZ2" for DP800 1.5-DP800 0.8. HAZ2s and FZs were not considered for RVEs since only the martensite phase was present in their microstructures.

The selection of the RVEs required for the micromechanical analysis is of great importance in the estimation of the flow curves to be obtained at the macro level. The selected RVE regions should be equal to the volume fraction of the phases contained in the material [32] and should be large enough to represent the material characteristic and small enough to reduce the computational time. Ramazani et al. [20] found that 25 μm was sufficient for the RVE size. Therefore, the RVE dimensions were taken as 30 μm in square form from the microstructures. Rectangular elements with a size of 100x100 mm were used in the FE mesh structure.

2D RVEs were first digitized from the real microstructures using ImageJ software. The regions were selected in such a way that the MVFs of the selected regions were close enough to the MVFs of the overall region. Then, the RVEs were generated with the object-oriented FE software OOF2, which was developed by the National Institute of Standards and Technology (NIST), calculating the local behavior and properties of microstructures in 2D. Randomly selected RVE regions for the base materials are given in Fig. 16. The red and black areas represent the ferrite and martensite phases, respectively.

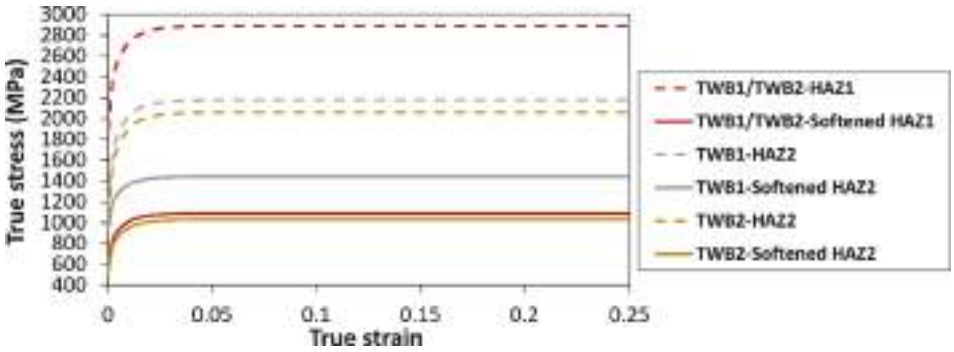

Fig. 23. Analytical flow curves of martensite and tempered martensite in TWB1 and TWB2.

Rectangular mesh structures of the RVEs selected from the microstructures of the base materials were generated in OOF2 software and are shown in Fig. 17. Considering that the RVE dimensions are 30 μm, the element sizes for all regions are 0.3 μm.

3.2. Definition of boundary conditions and loads

It was assumed that the RVEs are periodically distributed in the microstructure and the periodic boundary condition was used. To employ the periodic boundary condition on all 2D RVEs, a symmetric boundary condition was defined for the appropriate nodal points. Since the strain rate used in the study is $6.6x10^{-4}$ s^{-1} and the dimensions of the RVE element were at the micron level, the small explicit time step increased the analysis time. Therefore, an implicit integration scheme was used in the numerical simulations.

Boundary conditions applied to the RVEs are given in Fig. 18. For each RVE, a symmetrical boundary condition was defined on the left nodal points on the x-axis and the lower nodes on the y-axis, and a constant velocity loading boundary condition on the right nodes was defined with the Boundary_Prescribed_Motion keyword. It was assumed that the upper nodes of the RVE were located at the boundary of the microstructure and thus no boundary conditions were applied to these points.

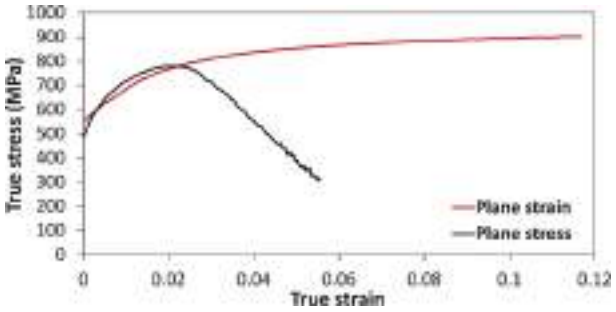

Fig. 24. Flow curves of DP800 1.5 obtained through the plane stress and plane strain elements.

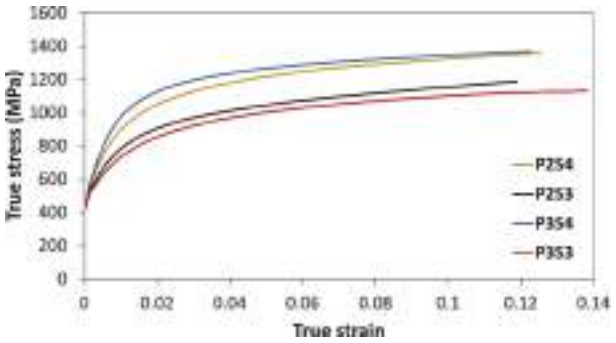

Fig. 25. Flow curves obtained from RVEs of the HAZ1 in TWB1 at different welding parameters.

3.3. Flow properties of distributed phases

The flow curves of the ferrite and martensite phases at room temperature were obtained using a dislocation-based strain hardening model proposed by Rodriguez and Gutiérrez [33]. The individual flow curves are defined by the following equation:

$$\sigma\,(\mathrm{MPa}) = \sigma_0 + \Delta\sigma + \alpha M \mu \sqrt{b}\sqrt{\frac{1-\exp\left(-Mk_2\varepsilon\right)}{k_2 L}} \tag{3}$$

where σ is the von Mises stress and ε is the equivalent plastic strain. The first term σ_0 describes the effects of alloying elements, while the second term Δσ describes the strengthening by precipitation or carbon in solution.

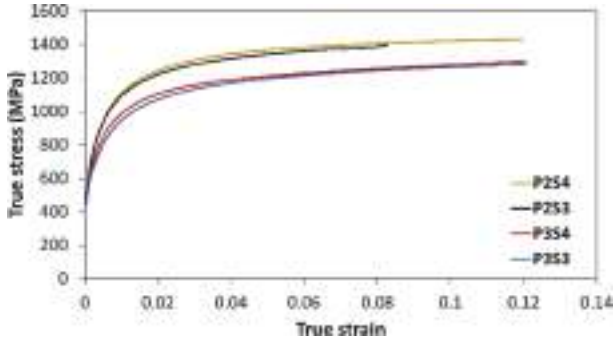

Fig. 26. Flow curves obtained from RVEs of the HAZ2 in TWB1 at different welding parameters.

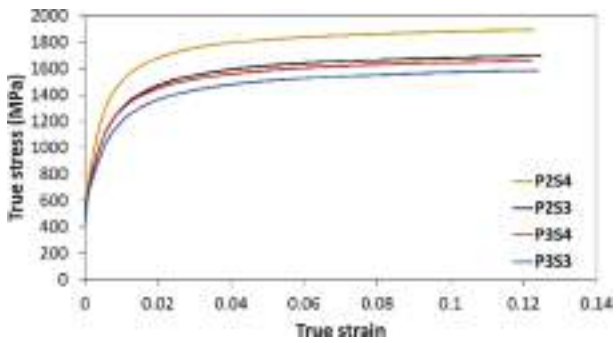

Fig. 27. Flow curves obtained from RVEs of the HAZ2 in TWB2 at different welding parameters.

Table 8
Equivalent plastic strain and von Mises stress distributions in micromechanical modeling of DP600 1.8 at various deformation levels.

	0.1 μm	0.5 μm	1 μm	3 μm
Equivalent plastic strain	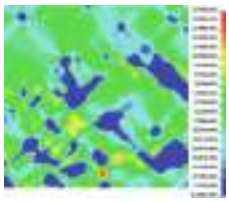	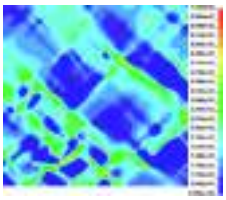	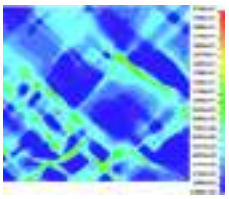	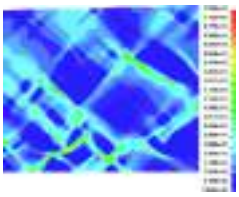
Von Mises stress	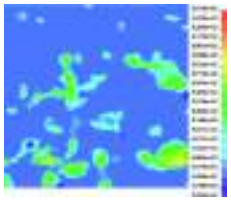	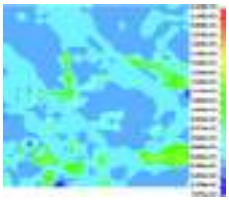	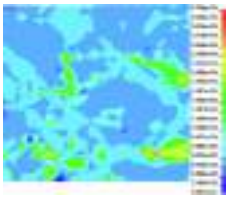	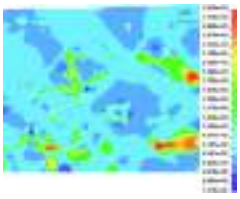

Table 9
Equivalent plastic strain and von Mises stress distributions in micromechanical modeling of DP800 1.5 at various deformation levels.

	0.1 μm	0.5 μm	1 μm	3 μm
Equivalent plastic strain	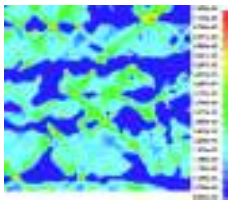	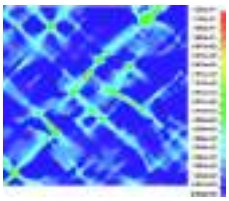	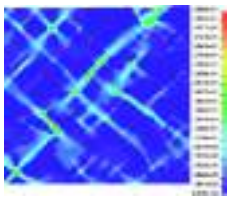	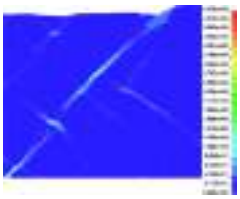
Von Mises stress	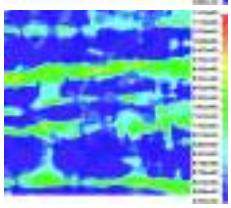	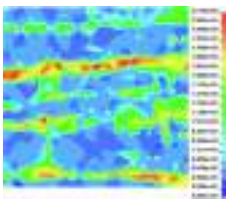	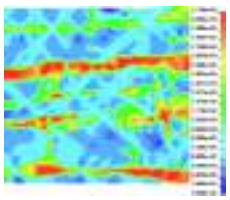	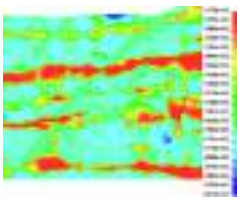

Table 10
Equivalent plastic strain and von Mises stress distributions in micromechanical modeling of DP800 0.8 at various deformation levels.

	0.1 μm	0.5 μm	1 μm	3 μm
Equivalent plastic strain	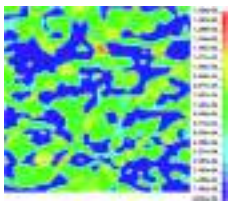	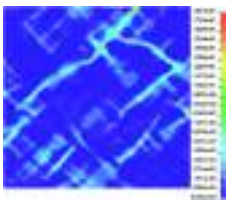	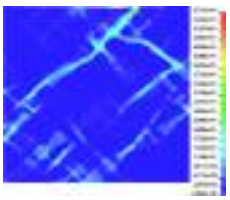	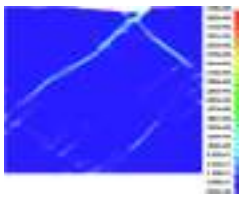
Von Mises stress	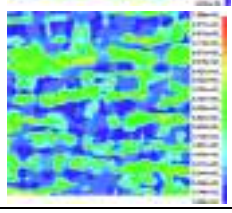	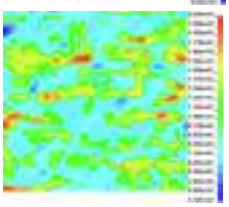	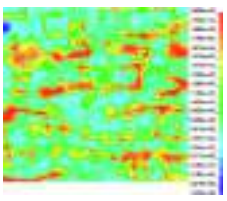	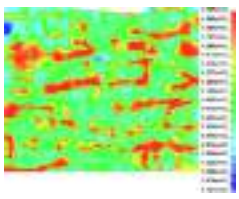

The values of parameters in the strain-dependent term in Eq. (3) were taken from Ramazani et al. [19] and are presented in Table 6. The term d_α represents the average ferrite grain size.

Since the contribution of carbon in ferrite and martensite phases to the strengthening is not the same, this effect is defined for each phase by the following equation:

$$\Delta\sigma(\mathrm{MPa}) = 5000(\%C_{ss}^{\ f}) \tag{4}$$

$$\Delta\sigma(\mathrm{MPa}) = 3065(\%C_{ss}^{\ m}) - 161 \tag{4}$$

where $\%C_{ss}^{\ f}$ and $\%C_{ss}^{\ m}$ denotes carbon contents (wt. %) in ferrite and martensite, respectively.

In this study, the flow curves of the phases were calculated using Eq. (3). It was assumed that the alloying elements in the σ_0 term were homogeneously distributed in the ferrite and martensite phases, and therefore, the amounts of alloying elements in the base materials were used for both phases. The carbon contents of ferrite and martensite in $\Delta\sigma$

Table 11
Equivalent plastic strain and von Mises stress distributions in micromechanical modeling of TWB1 at P2S3 welding parameter.

	DP600 1.8	Softened HAZ1	$HAZ1_{600}$
Equivalent plastic strain	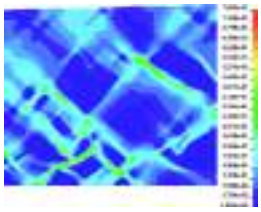	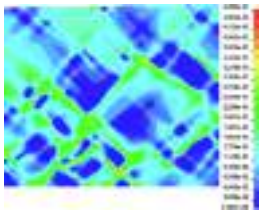	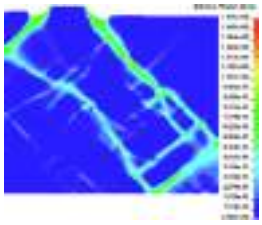
Von Mises stress	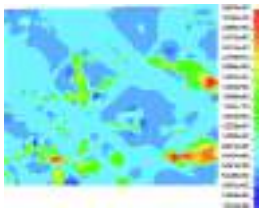	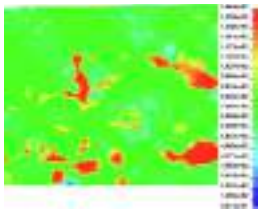	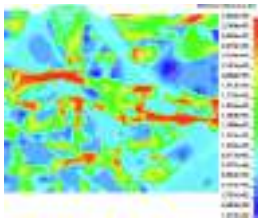
	$HAZ1_{800}$	Softened HAZ2	DP800 1.5
Equivalent plastic strain	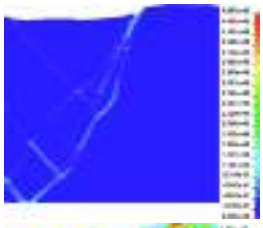	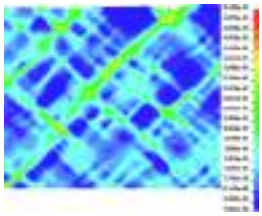	
Von Mises stress	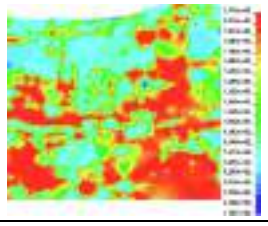	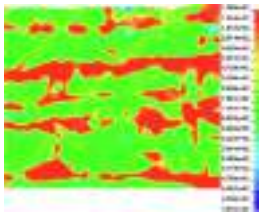	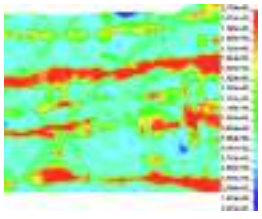

Table 12
Equivalent plastic strain and von Mises stress distributions in micromechanical modeling of TWB2 at P2S3 welding parameter.

	$HAZ1_{800}$	Softened HAZ2	DP800 0.8
Equivalent plastic strain	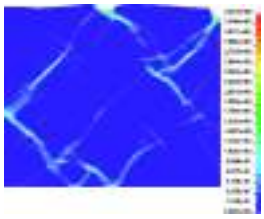	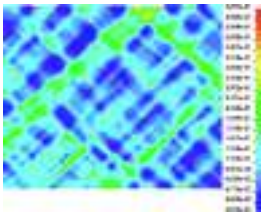	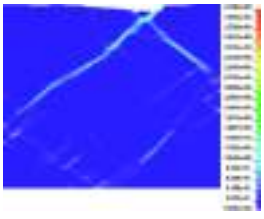
Von Mises stress	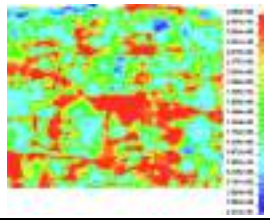	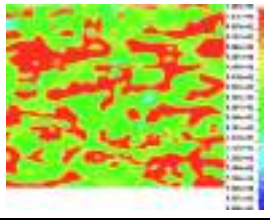	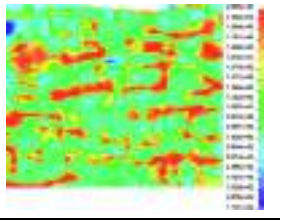

were determined separately. So, phase equilibrium calculations were performed using the thermodynamic modeling feature of JMatPro software. This software uses the CALPHAD (Calculations of Phase Diagrams) method to analyze and calculate the thermodynamic, kinetic, and thermophysical properties of materials from room temperature to liquid phase, time–temperature-transformation and continuous-cooling-transformation diagrams, stress–strain diagrams, etc. [34]. This software is widely used in the steel industry to obtain the required material properties in casting, forming, and heat treatment simulations [35].

DP steels are generally produced by intercritical annealing (a special heat treatment) of low/medium carbon steels. Since it was not known from which intercritical annealing temperatures of the steels used in the study were produced, firstly, the temperature values corresponding to

Fig. 28. Tensile test model and boundary conditions of base materials.

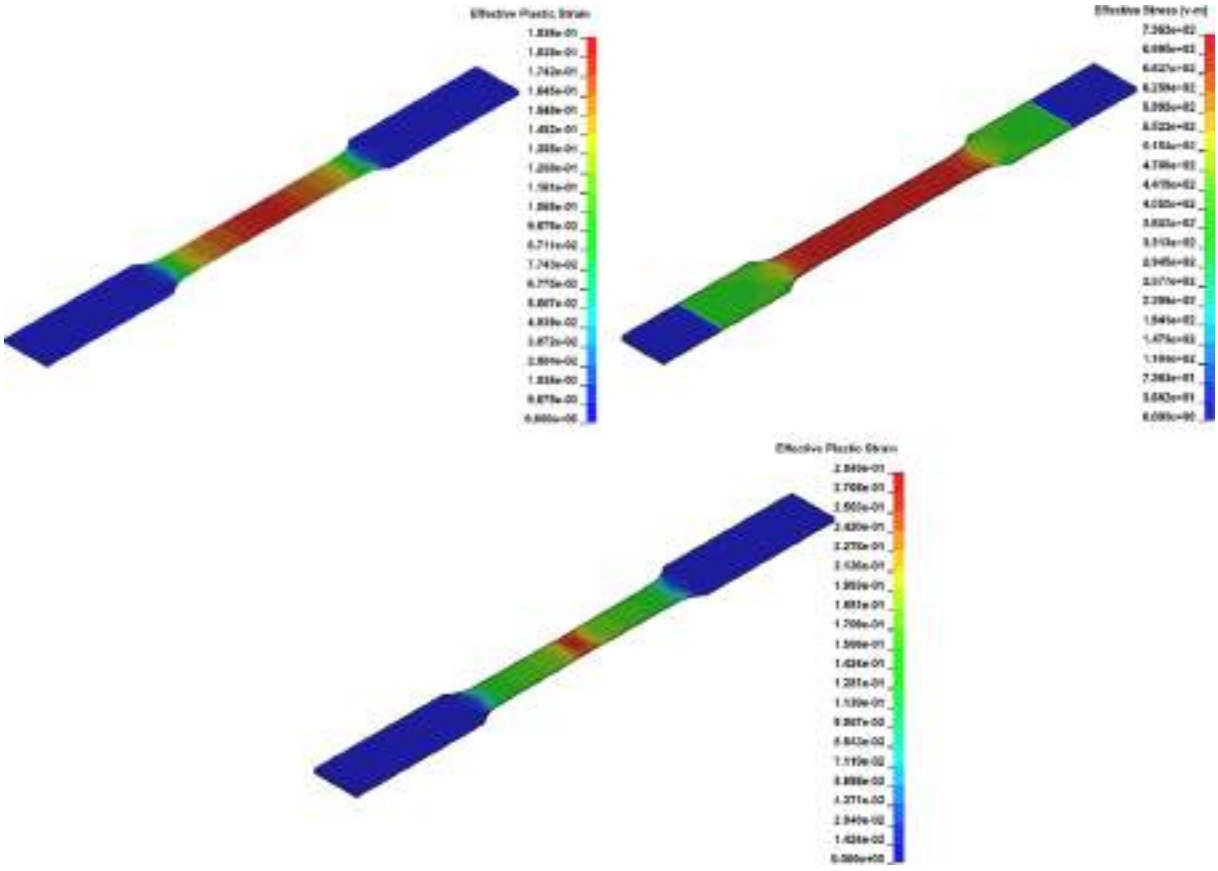

Fig. 29. Effective plastic strain (left-hand side image) and effective stress (right-hand side image) distributions at the necking, effective plastic strain distribution at fracture (bottom image) in the numerical analysis of DP600 1.8.

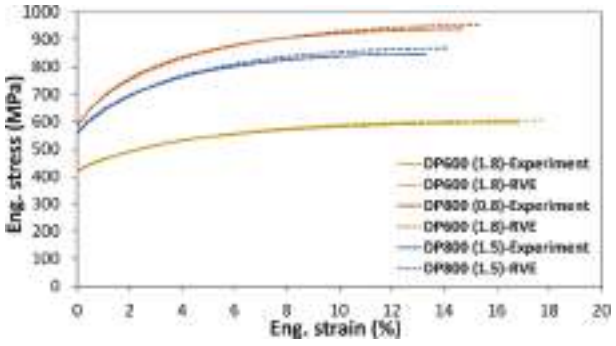

Fig. 30. Flow curves of the base materials obtained from experiments and micromechanical analyzes.

the MVFs in the microstructure of the base materials and the austenite contents were determined in the phase equilibrium calculations. Then, the amounts of carbon dissolved in the ferrite were obtained at the determined temperatures. Finally, the amounts of carbon in martensite were calculated by the following the mass balance equation [20]:

$$C_{DP} = V_m C_m + V_f C_f \quad (5)$$

where V_m and V_f are the martensite and ferrite volume fractions, respectively. C_m and C_f are the carbon content of martensite and ferrite, respectively, and C_{DP} is the nominal carbon content of DP steel.

Since the base materials used in the study were low carbon steels, the carbon contents in ferrite and martensite could not be determined by any experimental techniques. So, JMatPro software was used, and the annealing temperatures obtained for the base materials from the phase equilibrium calculations, the amount of carbon dissolved in the ferrite (C_f), and thus the carbon content in the martensite (C_m) calculated from Eq. (5) are presented in Table 7.

Flow curves of the ferrite and martensite phases in the microstructure of the base materials calculated by the dislocation density-based hardening model are shown in Fig. 19. As the carbon content in the martensite is the highest in DP600 1.8, the YS and flow behavior of the martensite phase is quite high compared to the other base materials. The flow behaviors of the martensite phases in DP800 1.5 and DP800 0.8 base materials are close to each other due to their near martensite carbon content, which is the most contributing factor to the strengthening

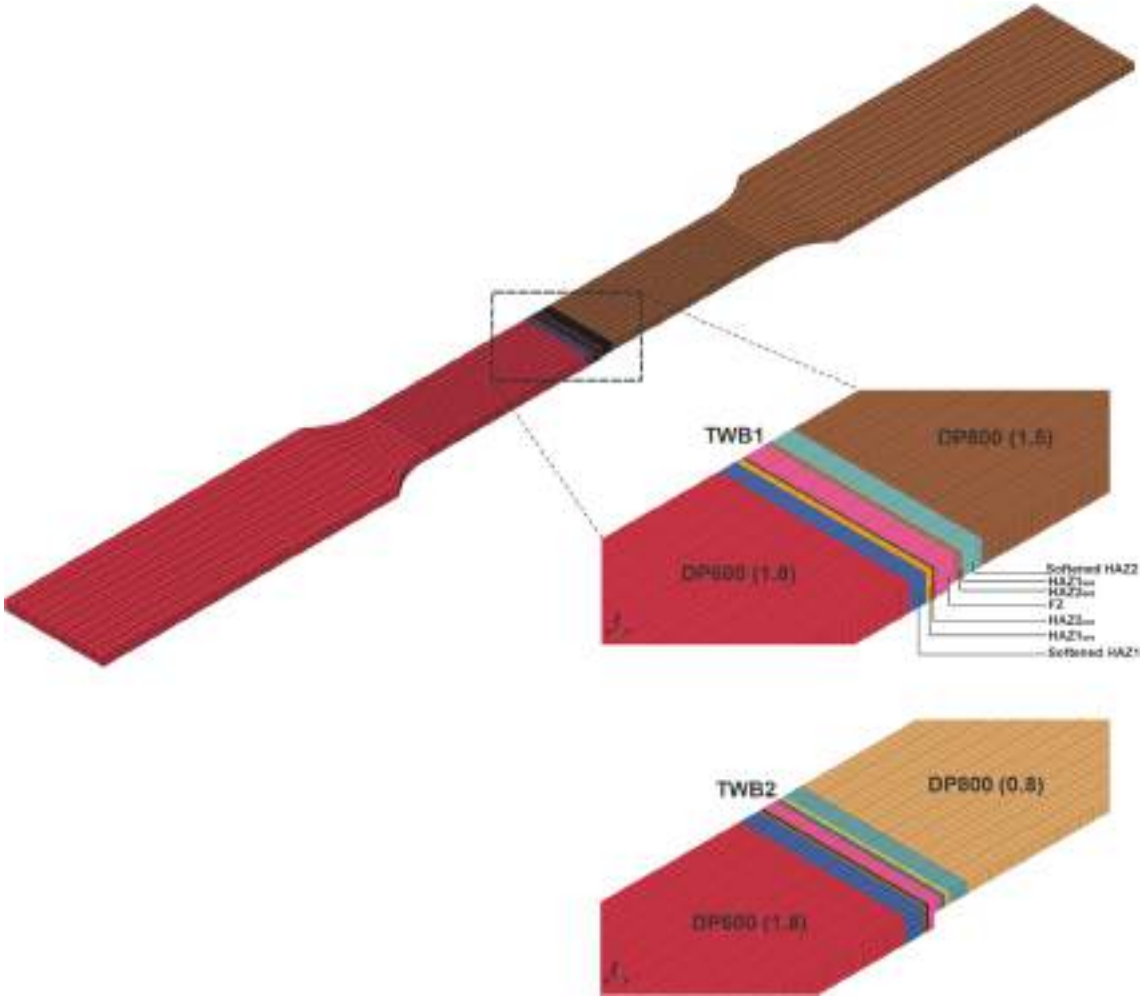

Fig. 31. Tensile test models of TWB1 and TWB2.

[36]. Besides, owing to the smaller ferrite grain size, the flow curve of the ferrite phase in DP800 0.8 is higher than that of the others.

Fig. 20 shows the flow curves of ferrite phases in $HAZ1_{600}$ of TWB1 at different welding parameters. Since the amount of carbon dissolved in ferrite is low, the flow behavior of ferrite is greatly affected by the ferrite grain size. As the effect of welding parameters on ferrite grain sizes in the HAZ1 is negligible, flow curves are quite close to each other.

Flow curves of the ferrite phases in $HAZ1_{800}$ of the TWB1 are shown in Fig. 21. Since the ferrite grain sizes in this zone changed more than $HAZ1_{600}$, a greater difference can be seen in the flow curves of $HAZ1_{800}$. Also, as shown in Fig. 22, unlike YSs, the flow curves of ferrite in $HAZ1_{800}$ of TWB2 show the same trend as in Fig. 20.

Analytical flow curves of martensite and tempered martensite in the TWB1 and TWB2 are given in Fig. 23. The dashed curves represent the martensite phase. The flow curves of tempered martensite in the Softened HAZs were calculated as half of the flow curves of the related martensite, as suggested by Mazinani and Poole [37].

3.4. Flow curves of representative volume elements

The flow curves of ferrite, martensite, and tempered martensite phases obtained using the dislocation density-based hardening model were defined with Mat_Piecewise_Linear_Plasticity, an elasto-plastic material model in Ls-Dyna. In this model, the density for all phases was taken as $7.83x10^{-9}$ tons/mm^3, and the elastic modulus and Poisson's ratio were taken as $2.07x10^5$ MPa and 0.29, respectively. The macroscopic stress components were calculated by averaging the volume of the microscopic components.

In the micromechanical analysis, plane stress and plane strain element assumptions were made for comparison. Micromechanical analysis was performed for the DP800 1.5 base material. Flow curves obtained after the homogenization process are shown in Fig. 24. In the flow curve obtained from the plane stress elements, it was observed that plastic instability started, and the stress decreased suddenly at insignificant deformation. So, it was determined that the plane stress element was insufficient for the 2D micromechanical analysis of DP steels, plane strain element was used for all analyzes.

The flow curves calculated from the RVEs of HAZ1 and HAZ2 of the TWB1 joined at different welding parameters are given in Fig. 25 and Fig. 26, respectively. Also, the flow curves of HAZ2 of the TWB2 are given in Fig. 27. It can be seen that the YSs do not depend on the welding parameters, whereas the UTSs in the flow curves of RVEs increase with MVF.

3.5. Stress and strain distributions in microstructures

Equivalent plastic strain and von Mises stress distributions obtained from 2D RVE micromechanical analyzes of the base materials at four different deformation levels are shown in Tables 8, 9, and 10. For all base materials, the ferrite phases plastically deform even at a low deformation value of 0.1 μm. At this deformation level, it can be seen that the plastic deformation in the martensite islands is very low. When the deformation level is 0.5 μm, slip bands of 45° are present in the ferrite phases along with the plastic deformation of the martensite

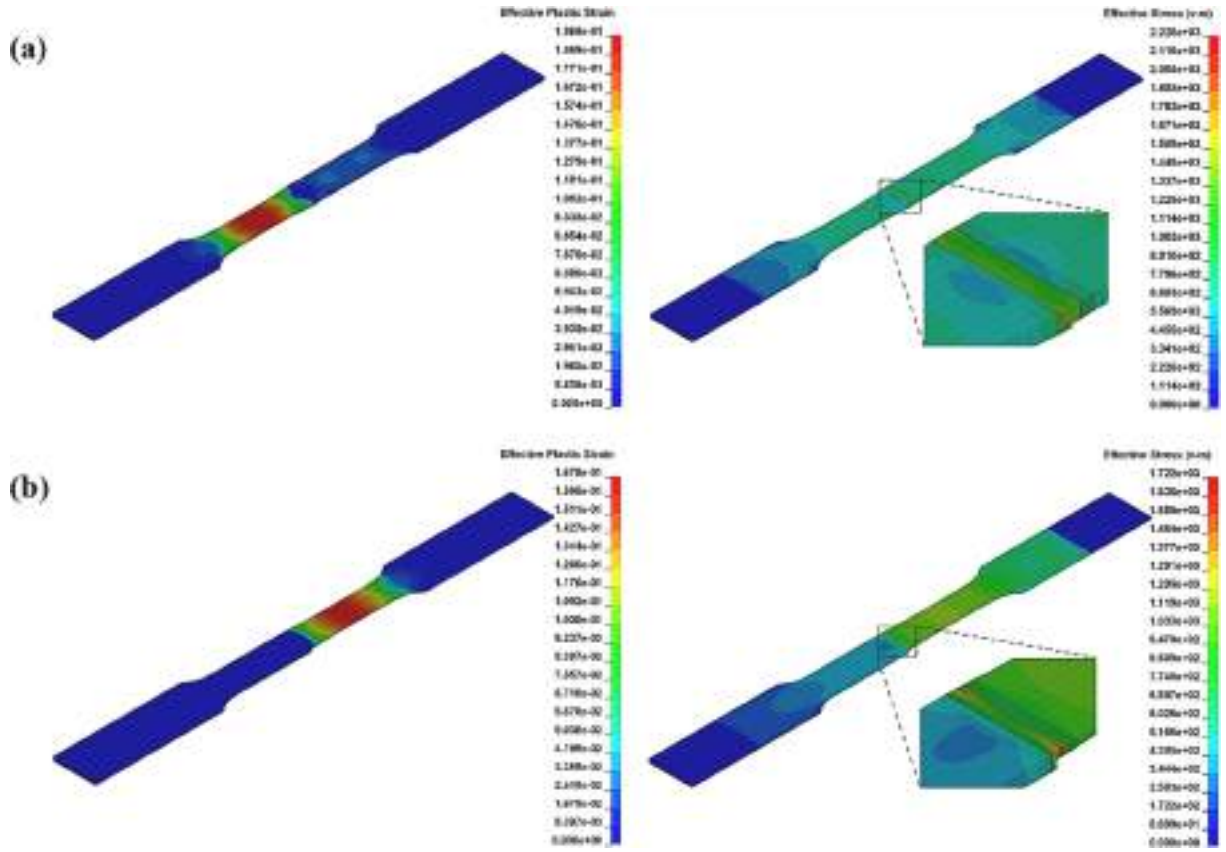

Fig. 32. Effective plastic strain (left hand side image) and effective stress (right hand side image) distributions at the necking in the tensile analysis of (a) TWB1, (b) TWB2.

islands. It was reported that DP steels have a shear damage mode [38,39] and plastic deformation occurs in the martensite phase during uniaxial tensile tests [40,41]. At the deformation levels of 1 μm and 3 μm, the plastic strain increases and is localized in the ferrite matrix. As shown in Table 8, the widest slip bands appear in DP600 1.8. The widths of slip bands decrease in both DP800 base materials (Tables 9 and 10).

The von Mises stress distribution in Table 8 shows that the stress in the martensite phases at deformation level of 0.1 μm was higher than the stress in the ferrite phases. However, the maximum stress of 652 MPa in the martensite phases is well below the YS of martensite (1900 MPa), exceeds the YS of ferrite (450 MPa). When the deformation level is 0.5 μm, the stress accumulates in the martensite phases. The low stress increase in the ferrite phases is due to the low hardenability of the ferrite phases. The stress increment in the martensite phases continues to increase significantly at the deformation level of 1 μm and peaks at 3 μm. When the stress distributions in the martensite of the base materials are compared, it is seen that the stresses are concentrated in certain regions of DP600 1.8, owing to the homogeneity of the martensite phases. Due to the high MVF of both DP800 base materials and the banded martensite phases, the stresses in the martensite phases at high deformation levels are more homogeneous.

The equivalent plastic strain and von Mises stress distributions in the weld zones of the TWB1 and TWB2 joined at P2S3 are given in Tables 11 and 12, respectively. The deformation is 3 μm in all analyzes. When the plastic strains of the softened HAZs and base materials are compared, it can be seen that the slip bands are wider in the softened HAZs, but the maximum plastic strain is higher in DP600 1.8. When the same comparison is made for stresses, more homogeneous stress distributions are present in tempered martensite in softened HAZs. Also, a similar homogeneity trend between $HAZ1_{600}$ and $HAZ1_{800}$ can be seen due to the different MVF in these zones.

3.6. Modeling of tensile tests

Uniaxial tensile specimens were modeled in 3D in Ls-Dyna to estimate the macroscopic flow curves of the base materials and TWB. The modeling was done using eight-node linear solid elements with a mesh size of 1 mm. The flow curves of the weld zones obtained from micromechanical analyzes were also defined by the Mat_Piecewise_Linear_Plasticity material model.

The model of the base materials used in the FE analysis is shown in Fig. 28 with the boundary conditions. In the model, the flow curves obtained from the RVEs of the base materials were defined for all solid elements. To obtain the flow behavior of the base materials from the uniaxial tensile analyzes performed in the Implicit integration scheme, the forces at the nodal points on the reduced section of the sample were measured and engineering stress–strain curves were calculated.

Effective plastic strain and stress distributions at the necking and fracture in the numerical analysis of DP600 1.8 are shown in Fig. 29. The maximum plastic strain (0.193) starts to localize throughout the center of the reduced section and the maximum stress (736 MPa) reaches the UTS (true stress) of the base material. At higher deformations, the plastic strain is localized in the center and the subsequent fracture occurs as in the tensile test experiment. Engineering stress-engineering strain curves obtained from the FE analyses of the base materials using the flow curves from RVEs with micromechanical analysis are shown in Fig. 30. A good correlation can be seen between the experimental and numerical curves.

Mesh structures of TWB1 and TWB2 are shown in Fig. 31. As can be seen, rectangular elements of different sizes were used in the HAZs and FZs. The element dimension used in the weld zones with the lowest width is 0.03 mm. The flow curves obtained from the RVEs of the base materials and weld zones were defined separately in the presented zones. To obtain the flow behavior of TWB from uniaxial tensile FE

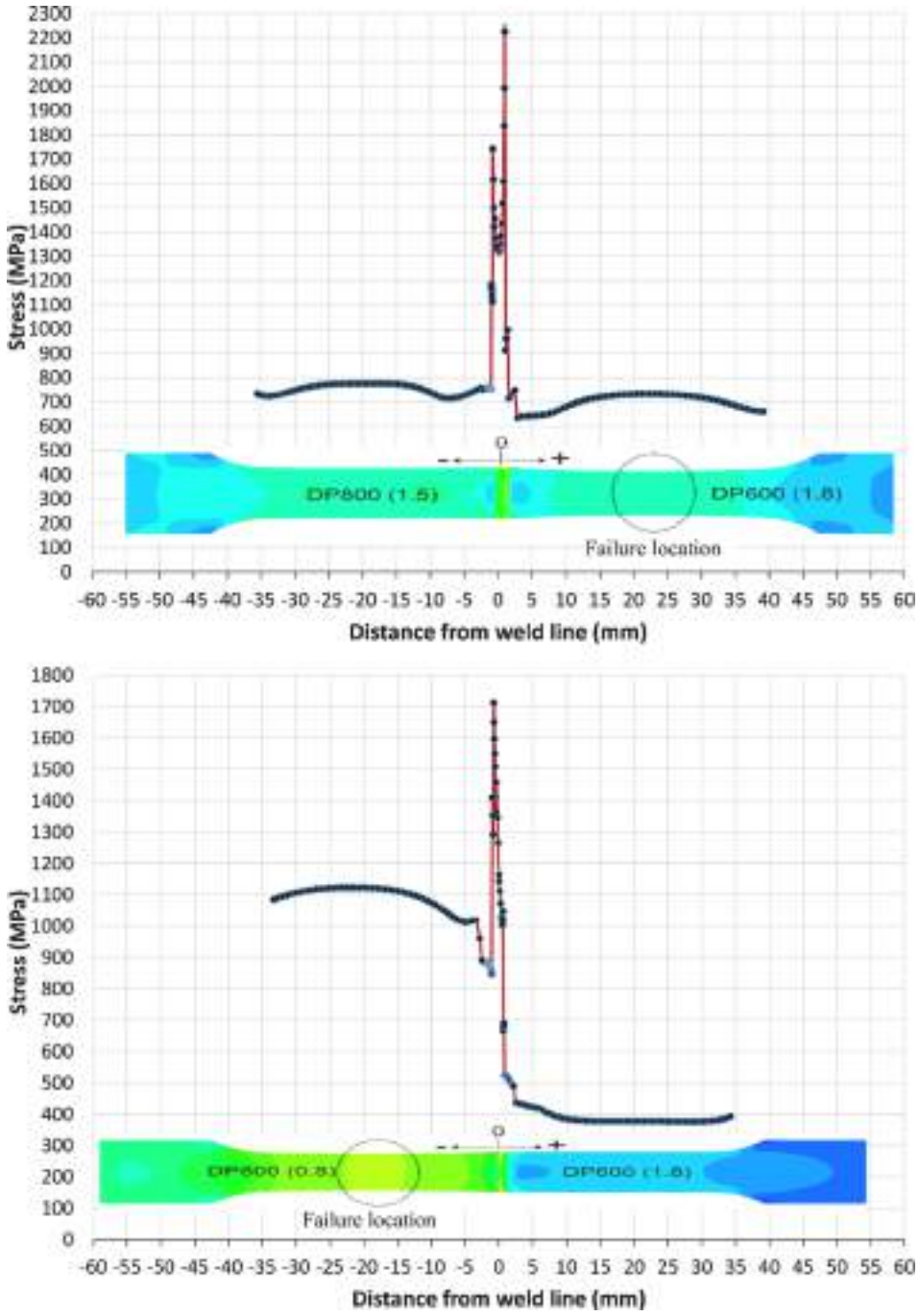

Fig. 33. Effective stress distribution and stress curve measured along the upper corner in tensile simulations of TWB1 and TWB2 at the necking.

analysis, the forces at the nodal points in the blank where the damage occurred were measured and engineering strain-engineering stress curves were calculated.

Fig. 32 shows the effective plastic strain and effective stress distributions at the necking in the tensile FE analysis of TWB1 and TWB2, respectively. At necking, the maximum plastic strain is localized in the center of the reduced section of DP600 1.8 and DP800 0.8 for TWB1 and TWB2, respectively. The fracture locations agree well with those of the experiments. In TWB1, the region where $HAZ2_{600}$ meets the sample corner carries the maximum stress among the other weld zones. However, in TWB2, because of the low cross-sectional area of DP800 0.8, the maximum stress appears in the region where $HAZ1_{800}$ meets the sample corner.

The effective stress distributions and the stress curves measured along the upper corner at the necking as a result of the tensile analysis of the TWB1 and TWB2 performed using the flow curves obtained from the RVEs are given in Fig. 33. It was realized that the maximum stresses occurred in the HAZS and FZs. Moreover, it was found that the stresses exceeded the YSs of the two base materials in both reduced sections of TWB1. The maximum stresses in DP800 1.5 and DP600 1.8 base materials were found to be 780 MPa and 740 MPa at the centers of the reduced sections, respectively. When the stress values were compared, it was observed that DP800 1.5 had undergone homogeneous plastic deformation, and no necking was present. However, in TWB1, the plastic strain localization appeared in DP600 1.8 due to the wide slip bands formed in its microstructure. In TWB2, although the same load was carried by DP600 1.8 and DP800 0.8, the stress distributions were different due to the difference in the cross-sectional areas. When the

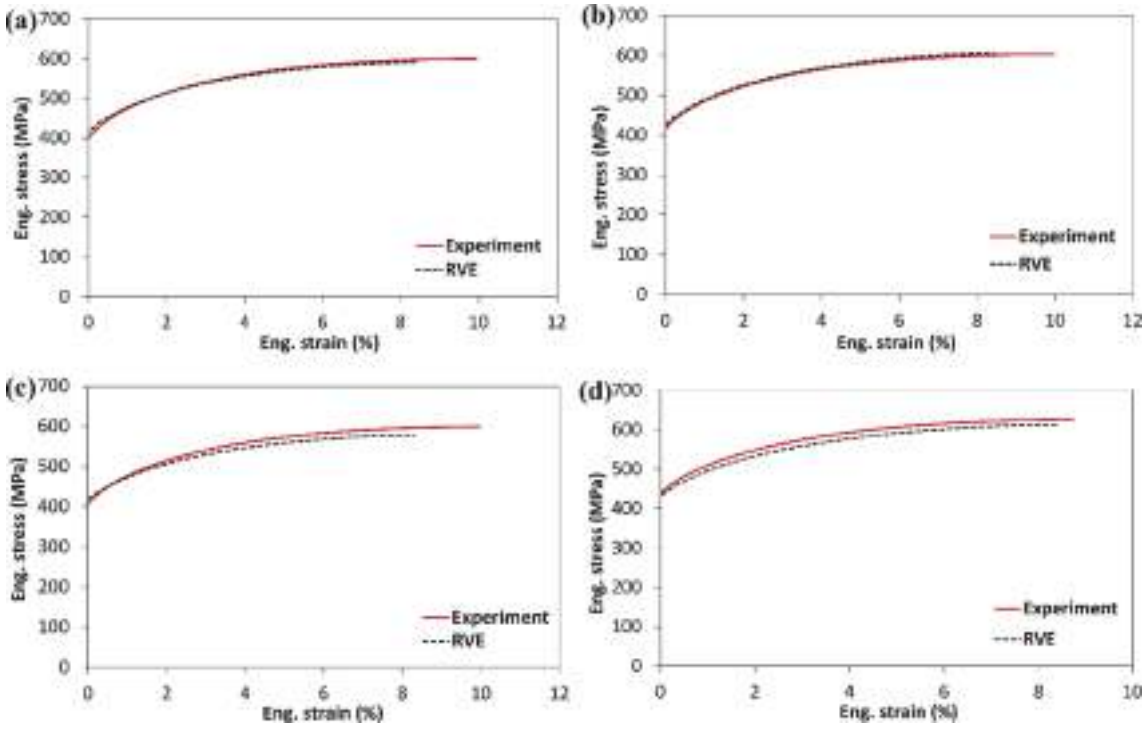

Fig. 34. Numerical and experimental flow curves of TWB1 at, (a) P2S3, (b) P2S4, (c) P3S3, (d) P3S4.

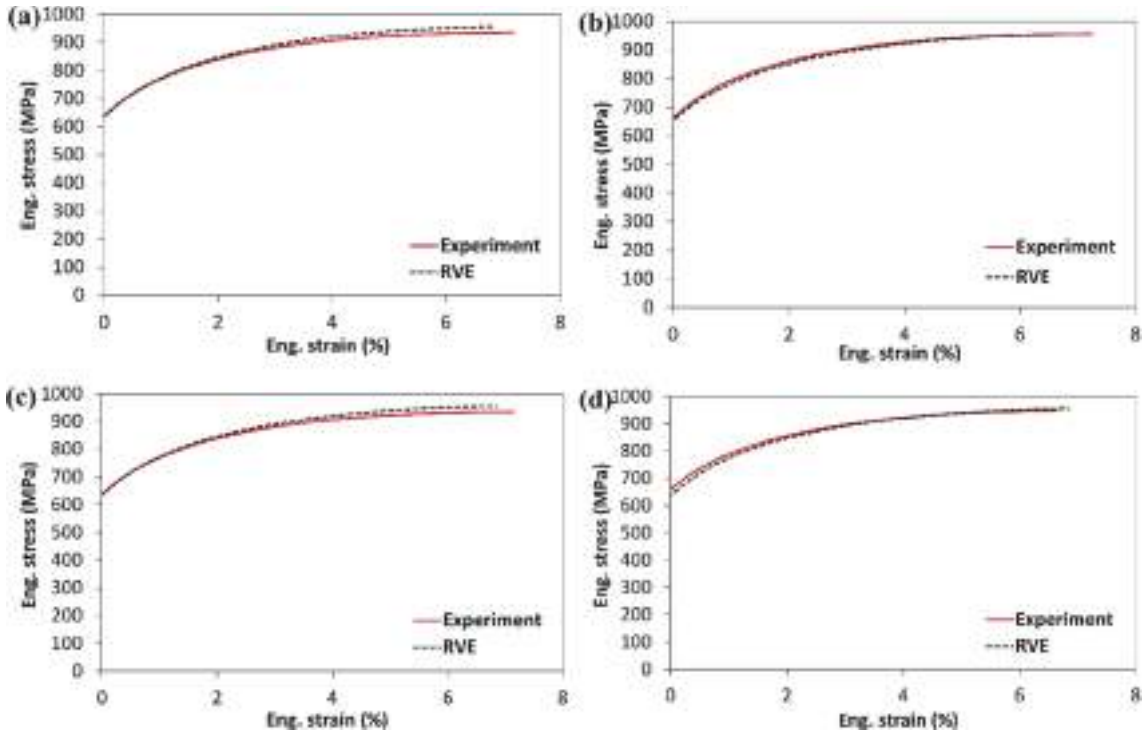

Fig. 35. Numerical and experimental flow curves of TWB2 at, (a) P2S3, (b) P2S4, (c) P3S3, (d) P3S4.

stress values were compared, it was observed that DP600 1.8 remained within the elastic limit, whereas DP800 0.8 had inhomogeneous plastic deformation.

Engineering stress-engineering strain curves obtained from the FE analyses of TWB1 and TWB2 at different welding parameters, using the flow curves from RVEs with micromechanical analysis are demonstrated in Fig. 34 and Fig. 35, respectively. It is seen that the numerical curves agree well with those of the experimental.

4. Conclusion

The composite microstructure of DP steels makes them a top priority for automotive manufacturers in the material selection process. However, the future forming performance of TWB is significantly affected by

degradation in the mechanical properties of DP steels. Therefore, in this study, the effect of the laser welding process on the final mechanical properties of TWB was investigated by 2D micromechanical modeling method considering microstructural changes, and the macro-flow behaviors of TWB were predicted.

Since laser welding affected the temperature gradients and thus the cooling rate in the TWB, different HAZs were obtained in the weld zones. In the microstructures of TWB1 and TWB2, FZs were completely composed of lath martensite due to high heat input and high cooling rate characteristics. As the cooling rate decreased, the martensite transformed into plate form in the weld zone next to the FZ (HAZ2s). Low heat input and high welding speed tempered the martensite phases in the base materials, consequently, the widths of the softened HAZs were low. High Mn and Si contents of DP800 1.5 and DP800 0.8 resulted in banded ferrite and martensite phases in the HAZ1s, as in the base materials.

Depending on the thickness ratios and tensile strengths of the TWB, the damage occurred in different base materials. The ductility of the TWB1 and TWB2 decreased by 32 % and 43 %, respectively, compared to the base materials. The effect of welding speed on the strength values of TWB was higher than laser power.

In micromechanical analyzes of base materials, ferrite phases had plastic strain even at a low deformation value of 0.1 μm. When the deformation level reached 0.5 μm, plastic deformation occurred in martensite, and slip bands of 45° were formed in the ferrite/martensite interfaces. Plastic strain localizations appeared in ferrite upon a further increase in deformation. The widest slip bands occurred in DP600 1.8 with the largest ferrite grains. Therefore, coarse ferrite grains had undergone plastic deformation more easily.

In the tensile analyzes performed for the base materials, the effective plastic strain and effective stress values were obtained close to the experimental data, and the flow curves were in good agreement with the experimental flow curves. Therefore, it is suggested that the 2D RVE method is an effective method for evaluating the local and macro-behavior of DP steels and TWB by accurately determining the parameters in the dislocation density-based hardening model.

CRediT authorship contribution statement

Ekrem Öztürk: Conceptualization, Methodology, Investigation, Writing – review & editing, Visualization. **Hüseyin Arıkan:** Supervision, Conceptualization, Funding acquisition, Methodology.

Declaration of Competing Interest

The authors declare that they have no known competing financial interests or personal relationships that could have appeared to influence the work reported in this paper.

Data availability

The authors do not have permission to share data.

Acknowledgments

This paper was extracted from a Ph.D. thesis (No. 686528) submitted to the Graduate School of Natural and Applied Sciences of Necmettin Erbakan University. The authors gratefully acknowledge the funding from the Scientific Research Projects (BAP) Coordination Unit of Necmettin Erbakan University [grant number 181431001].

References

[1] K. Bandyopadhyay, M.-G. Lee, S.K. Panda, P. Saha, J. Lee, Formability assessment and failure prediction of laser welded dual phase steel blanks using anisotropic plastic properties, Int. J. Mech. Sci. 126 (2017) 203–221, https://doi.org/10.1016/j.ijmecsci.2017.03.022.

[2] G. Moeini, A. Ramazani, J. Hildebrand, C. Roessler, C. Koenke, Study of the effect of microstructural variation on the low cycle fatigue behavior of laser welded DP600 steel: Simulation and experimental validation, Mater. Sci. Eng., A 730 (2018) 232–243, https://doi.org/10.1016/j.msea.2018.06.004.

[3] D. Anand, D.L. Chen, S.D. Bhole, P. Andreychuk, G. Boudreau, Fatigue behavior of tailor (laser)-welded blanks for automotive applications, Mater. Sci. Eng., A 420 (2006) 199–207, https://doi.org/10.1016/j.msea.2006.01.075.

[4] M. Merklein, M. Johannes, M. Lechner, A. Kuppert, A review on tailored blanks—Production, applications and evaluation, J. Mater. Process. Technol. 214 (2014) 151–164, https://doi.org/10.1016/j.jmatprotec.2013.08.015.

[5] R.S. Korouyeh, H.M. Naeini, M.J. Torkamany, G.H. Liaghat, Experimental and theoretical investigation of thickness ratio effect on the formability of tailor welded blank, Opt. Laser Technol. 51 (2013) 24–31, https://doi.org/10.1016/j.optlastec.2013.02.016.

[6] A. Grajcar, M. Morawiec, M. Różański, S. Stano, Twin-spot laser welding of advanced high-strength multiphase microstructure steel, Opt. Laser Technol. 92 (2017) 52–61, https://doi.org/10.1016/j.optlastec.2017.01.011.

[7] R.S. Sharma, P. Molian, Weldability of advanced high strength steels using an Yb: YAG disk laser, J. Mater. Process. Technol. 211 (2011) 1888–1897, https://doi.org/10.1016/j.jmatprotec.2011.06.009.

[8] A.A. Zadpoor, J. Sinke, R. Benedictus, Mechanics of tailor welded blanks: an overview, Key Eng. Mater. 344 (2007) 373–382, https://doi.org/10.4028/www.scientific.net/KEM.344.373.

[9] U. Reisgen, M. Schleser, O. Mokrov, E. Ahmed, Optimization of laser welding of DP/TRIP steel sheets using statistical approach, Opt. Laser Technol. 44 (2012) 255–262, https://doi.org/10.1016/j.optlastec.2011.06.028.

[10] ArcelorMittal, ArcelorMittal Tailored Blanks catalogue, n.d. https://fce.arcelormittal.com/repository/fce/Tailored_Blanks/Catalogue-Chapter1.pdf (accessed August 17, 2022).

[11] C.Y. Kang, T.K. Han, B.K. Lee, J.K. Kim, Characteristics of Nd: YAG laser welded 600MPa grade TRIP and DP steels, in, Materials Science Forum, Trans Tech Publ (2007) 3967–3972, https://doi.org/10.4028/www.scientific.net/MSF.539-543.3967.

[12] M. Uchihara, K. Fukui, Tailored Blanks of High Strength Steels—Comparison of Welding Processes, Welding in the World. 46 (2002) 41–48, https://doi.org/10.1007/BF03263389.

[13] N. Sreenivasan, M. Kuntz, Y. Zhou, Influence of laser welding on the formability of AHSS steels, in: Materials Science and Technology Conference and Exhibition, MS and T'07-"Exploring Structure, Processing, and Applications Across Multiple Materials Systems", 2007: pp. 3141–3152.

[14] M. Xia, E. Biro, Z. Tian, Y.N. Zhou, Effects of heat input and martensite on HAZ softening in laser welding of dual phase steels, ISIJ Int. 48 (2008) 809–814, https://doi.org/10.2355/isijinternational.48.809.

[15] X. Sun, K.S. Choi, W.N. Liu, M.A. Khaleel, Predicting failure modes and ductility of dual phase steels using plastic strain localization, Int. J. Plast. 25 (2009) 1888–1909, https://doi.org/10.1016/j.ijplas.2008.12.012.

[16] X. Sun, K.S. Choi, A. Soulami, W.N. Liu, M.A. Khaleel, On key factors influencing ductile fractures of dual phase (DP) steels, Mater. Sci. Eng., A 526 (2009) 140–149, https://doi.org/10.1016/j.msea.2009.08.010.

[17] A. Ramazani, A. Schwedt, A. Aretz, U. Prahl, W. Bleck, Characterization and modelling of failure initiation in DP steel, Comput. Mater. Sci. 75 (2013) 35–44, https://doi.org/10.1016/j.commatsci.2013.04.001.

[18] X. Wei, S.A. Asgari, J.T. Wang, B.F. Rolfe, H.C. Zhu, P.D. Hodgson, Micromechanical modelling of bending under tension forming behaviour of dual phase steel 600, Comput. Mater. Sci. 108 (2015) 72–79, https://doi.org/10.1016/j.commatsci.2015.06.012.

[19] A. Ramazani, K. Mukherjee, A. Abdurakhmanov, U. Prahl, M. Schleser, U. Reisgen, W. Bleck, Micro–macro-characterisation and modelling of mechanical properties of gas metal arc welded (GMAW) DP600 steel, Mater. Sci. Eng., A 589 (2014) 1–14, https://doi.org/10.1016/j.msea.2013.09.056.

[20] A. Ramazani, K. Mukherjee, H. Quade, U. Prahl, W. Bleck, Correlation between 2D and 3D flow curve modelling of DP steels using a microstructure-based RVE approach, Mater. Sci. Eng., A 560 (2013) 129–139, https://doi.org/10.1016/j.msea.2012.09.046.

[21] D. Dong, Y. Liu, Y. Yang, J. Li, M. Ma, T. Jiang, Microstructure and dynamic tensile behavior of DP600 dual phase steel joint by laser welding, Mater. Sci. Eng., A 594 (2014) 17–25, https://doi.org/10.1016/j.msea.2013.11.047.

[22] B.L. Ennis, C. Bos, M.P. Aarnts, P.D. Lee, E. Jimenez-Melero, Work hardening behaviour in banded dual phase steel structures with improved formability, Mater. Sci. Eng., A 713 (2018) 278–286, https://doi.org/10.1016/j.msea.2017.12.078.

[23] B. Krebs, L. Germain, A. Hazotte, M. Gouné, Banded structure in Dual Phase steels in relation with the austenite-to-ferrite transformation mechanisms, J. Mater. Sci. 46 (2011) 7026–7038, https://doi.org/10.1007/s10853-011-5671-9.

[24] ASTM E562-19e1, Standard Test Method for Determining Volume Fraction by Systematic Manual Point Count, (2013). https://doi.org/10.1520/E0562-19E01.

[25] C.A. Schneider, W.S. Rasband, K.W. Eliceiri, NIH Image to ImageJ: 25 years of image analysis, Nat Methods. 9 (2012) 671–675, https://doi.org/10.1038/nmeth.2089.

[26] ASTM E112-13, Standard Test Methods for Determining Average Grain Size, (2013). https://doi.org/10.1520/E0112-13R21.

[27] ASTM E8/E8M-16, Standard Test Methods for Tension Testing of Metallic Materials, (2016). 10.1520/E0008_E0008M-16.

[28] E. Pan, H. Di, G. Jiang, C. Bao, Effect of heat treatment on microstructures and mechanical properties of hot-dip galvanized DP steels, Acta Metallurgica Sinica (English Letters). 27 (2014) 469–475, https://doi.org/10.1007/s40195-014-0066-y.

[29] N.H. Abid, R.K. Abu Al-Rub, A.N. Palazotto, Micromechanical finite element analysis of the effects of martensite morphology on the overall mechanical behavior of dual phase steel, Int. J. Solids Struct. 104–105 (2017) 8–24, https://doi.org/10.1016/j.ijsolstr.2016.11.005.
[30] R.K. Abu Al-Rub, M. Ettehad, A.N. Palazotto, Microstructural modeling of dual phase steel using a higher-order gradient plasticity–damage model, Int. J. Solids Struct. 58 (2015) 178–189, https://doi.org/10.1016/j.ijsolstr.2014.12.029.
[31] J. Zhang, H. Di, Y. Deng, R.D.K. Misra, Effect of martensite morphology and volume fraction on strain hardening and fracture behavior of martensite–ferrite dual phase steel, Mater. Sci. Eng., A 627 (2015) 230–240, https://doi.org/10.1016/j.msea.2015.01.006.
[32] E. Espinosa, A. Sardar, C.H.M. Simha, A. Bardelcik, Realistic morphology-based Representative Volume Elements for dual-phase steels, Mech. Mater. 160 (2021), 103961, https://doi.org/10.1016/j.mechmat.2021.103961.
[33] R. Rodriguez, I. Gutiérrez, Unified formulation to predict the tensile curves of steels with different microstructures, in: Materials Science Forum, Trans Tech Publications Ltd, Zurich-Uetikon, Switzerland, 2003, pp. 4525–4530.
[34] N. Saunders, U.K.Z. Guo, X. Li, A.P. Miodownik, J.-P. Schillé, Using JMatPro to model materials properties and behavior, Jom. 55 (2003) 60–65, https://doi.org/10.1007/s11837-003-0013-2.
[35] U. Diekmann, Calculation of steel data using JMatPro, COMAT2012. 21 (2012) 11.
[36] M. Amirmaleki, J. Samei, D.E. Green, I. van Riemsdijk, L. Stewart, 3D micromechanical modeling of dual phase steels using the representative volume element method, Mech. Mater. 101 (2016) 27–39, https://doi.org/10.1016/j.mechmat.2016.07.011.
[37] M. Mazinani, W.J. Poole, Effect of martensite plasticity on the deformation behavior of a low-carbon dual-phase steel, Metallurgical and Materials Transactions A. 38 (2007) 328–339, https://doi.org/10.1007/s11661-006-9023-3.
[38] A.C. Darabi, H.R. Chamani, J. Kadkhodapour, A.P. Anaraki, A. Alaie, M. R. Ayatollahi, Micromechanical analysis of two heat-treated dual phase steels: DP800 and DP980, Mech. Mater. 110 (2017) 68–83, https://doi.org/10.1016/j.mechmat.2017.04.009.
[39] J. Liao, J.A. Sousa, A.B. Lopes, X. Xue, F. Barlat, A.B. Pereira, Mechanical, microstructural behaviour and modelling of dual phase steels under complex deformation paths, Int. J. Plast. 93 (2017) 269–290, https://doi.org/10.1016/j.ijplas.2016.03.010.
[40] M. Azuma, S. Goutianos, N. Hansen, G. Winther, X. Huang, Effect of hardness of martensite and ferrite on void formation in dual phase steel, Mater. Sci. Technol. 28 (2012) 1092–1100, https://doi.org/10.1179/1743284712Y.0000000006.
[41] M. Calcagnotto, D. Ponge, E. Demir, D. Raabe, Orientation gradients and geometrically necessary dislocations in ultrafine grained dual-phase steels studied by 2D and 3D EBSD, Mater. Sci. Eng., A 527 (2010) 2738–2746, https://doi.org/10.1016/j.msea.2010.01.004.